



An Overview of Selected Current Approaches to the Characterization of Aqueous Inorganic Clusters

Journal:	<i>Dalton Transactions</i>
Manuscript ID:	DT-PER-04-2015-001268.R1
Article Type:	Perspective
Date Submitted by the Author:	23-Jun-2015
Complete List of Authors:	<p>Jackson Jr, Milton; Thermo Fisher Scientific , ; University of Oregon, Department of Chemistry Kamunde-Devonish, Maisha; University of Oregon, Hammann, Blake; Washington University at St. Louis, Department of Chemistry Wills, Lindsay; Oregon State University, Department of Chemistry Fullmer, Lauren; Oregon State University, Department of Chemistry Hayes, Sophia; Washington University at St. Louis, Department of Chemistry Cheong, Paul; Oregon State University, Chemistry Casey, William; University of California, Department of Chemistry Nyman, May; Oregon State University, Department of Chemistry Johnson, Darren; University of Oregon,</p>

An Overview of Selected Current Approaches to the Characterization of Aqueous Inorganic Clusters

Milton N. Jackson, Jr.,^a Maisha K. Kamunde-Devonish,^a Blake A. Hammann,^b Lindsay A. Wills,^c Lauren B. Fullmer,^c Sophia E. Hayes,^{*,b} Paul H.-Y. Cheong,^{*,c} William H. Casey,^{*,d} May D. Nyman,^{*,c} and Darren W. Johnson^{*,a}

ABSTRACT

This **Perspective** article highlights some of the traditional and non-traditional analytical tools that are presently used to characterize aqueous inorganic nanoscale clusters and polyoxometalate ions. The techniques discussed in this article include nuclear magnetic resonance spectroscopy (NMR), small angle x-ray scattering (SAXS), dynamic and phase analysis light scattering (DLS and PALS), Raman spectroscopy, and quantum mechanical computations (QMC). For each method we briefly describe how it functions and illustrate how these techniques are used to study cluster species in the solid state and in solution through several representative case studies. In addition to highlighting the utility of these techniques, we also discuss limitations of each approach and measures that can be applied to circumvent such limits as it pertains to aqueous inorganic cluster characterization.

1. INTRODUCTION

There are many types of widely-studied nanomaterials that are termed ‘clusters’, and a variety of characterization techniques have been applied to determine their structure in solution and the solid state. This Perspective highlights some of the current and emerging approaches to cluster characterization in the context of several case studies on hydrated nanoscale clusters. We begin with a short discussion establishing what constitutes a “cluster” for the purposes of this

review. A cluster is broadly defined as a species that contains several metal cations (usually 4 or more, but may contain up to several hundred) linked by ligands, and surface passivated or functionalized by additional ligands that 1) are similar to the linking ligands, or 2) organic ligands of a different nature. The ligands are most often Group 16 dianions O^{2-} , S^{2-} , or Se^{2-} , or their protonated derivatives¹ and we are limiting our focus to hydrated inorganic clusters composed only of ligands derived from water (aqua ligands), including H_2O , OH^- , or O^{2-} . For completeness, we also include tetrahedral oxoanions such as $PO_4H_x^{(3-x)-}$, $P_2O_7H_x^{(4-x)-}$, and SO_4^{2-} that may serve as counterions and/or assist in cluster coordination. There are many clusters that contain aqua ligands in their interior; but are surface-passivated by organic ligands including alkoxides, carboxylates, amines, etc.^{2,3} Many of the characterization techniques described herein would be suitable for these clusters, but they are not a focus of the case studies in this review. We also differentiate between molecular clusters and non-molecular clusters and provide studies of both categories.

Molecular clusters have a discrete and absolute formula. Molecular clusters generally self-assemble in aqueous solution through pH control, concentration effects, counterion influence, etc, and are subsequently purified via selective crystallization. Clusters that fall into this category are predominantly the Group V/VI polyoxometalates (POMs)⁴ that are stabilized by the ubiquitous multiply bonded oxo ligand on the surface of the cluster. Due to the strong and relatively inert $M=O$ bond ($M = V, Nb, Ta, Mo, \text{ or } W$) of most POMs, the propensity for agglomeration and/or precipitation via hydrolysis and condensation reactions is not of prominent concern. While POMs carry a negative charge (polyoxoanions); others such as Group 13 metals (such as Al and Ga) form polyoxocations.⁵ These clusters tend to have similar nanoscale sizes as POMs (1-2 nm), but the Group 13 polyoxocations do not possess terminal $M=O$ bonds and the

ligands are typically protic species such as OH^- and H_2O instead of the oxo ligand of the POMs, thus leading to their overall positive charge. What differentiates these clusters from the non-molecular clusters discussed below is that they are sufficiently stable to condensation reactions that would lead to aggregation, allowing these species to be isolated and studied in solution over certain pH and concentration ranges. Moreover, they can be crystallized as discrete and monodisperse entities. These are the properties that the POMs and Group 13 polyoxocations share uniquely, and few other classes of metal oxo clusters have been identified that provide this level of stability in solution.

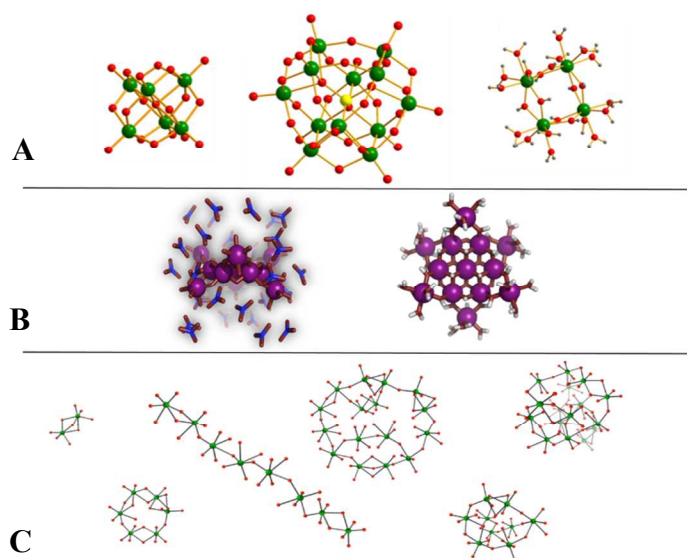


Figure 1. Examples of discrete metal-oxo/hydroxo clusters (A and B) and polynuclear ‘prenucleation’ clusters (C). From left to right: A) The Lindqvist ion $[\text{M}_6\text{O}_{19}]^x-$ ($\text{M} = \text{Mo}, \text{W}, \text{Nb}, \text{Ta}$; $x = 2-8$), the Keggin ion $[\text{TM}_{12}\text{O}_{40}]^y-$ ($\text{M} = \text{Mo}, \text{W}, \text{Nb}$; $\text{T} = \text{Al}, \text{Si}, \text{P}$, etc. $x = 3-16$), $[\text{M}_8(\text{OH})_8(\text{H}_2\text{O})_{12}]^{8+}$ ($\text{M} = \text{Zr}, \text{Hf}$). B) Side and planar projections of the flat tridecamer $[\text{M}_{13}(\text{OH})_{24}(\text{H}_2\text{O})_{24}]^{15+}$ ($\text{M} = \text{Al}, \text{Ga}, \text{In}$) with and without the counterions present. The hydrogen atoms are removed in the side projection to make to view easier to look at. C) Prenucleation clusters illustrating the nondiscrete linking and assembly of metal-oxo/hydroxyl/aqua octahedra through corner-sharing, edge-sharing and face-sharing. This is illustrative of the process that takes place with hydrolysis and condensation of metals that do not form discrete, isolatable clusters without the use of protective ligands. (i.e. open shell transition metals including Fe, Ni, Mn). Color legend: Figure 1A and 1C - Metal atoms = green (yellow for the central tetrahedral metal ion in the keggion ion), oxygen = red, hydrogen = white. For Figure 1B - Metal atoms = purple, oxygen = red, nitrogen = blue, hydrogen = white.

In contrast to molecular clusters, non-molecular clusters (also referred to as pre-nucleation clusters or inorganic polymers) are far less understood. These are generally a mixture of soluble species, anionic or cationic, that are small aggregates or nuclei that form prior to precipitation of

a metal oxide or related solid. They form by essentially the same aqueous chemistry of pH controlled hydrolysis and condensation reactions that provide both the POMs and polyoxocations. These pre-nucleation clusters can be considered the intermediate state between a monomeric metal cation and a precipitated solid. They are not well understood because they difficult to isolate for study, are highly reactive and therefore dynamic, transient, and polydispersed. These characteristics present considerable challenges towards characterization. However, understanding how both natural and synthetic materials form is critical in order to controllably formulate new nanomaterials. In theory, any metal on the periodic table can possess this intermediate state between monomer and metal oxide solid, but few such systems have been studied in detail. Most of the pre-nucleation clusters that have been investigated to date are those in the natural world including aluminosilicates, iron oxyhydroxide (FeOOH) and calcium carbonate [Ca(CO₃)].⁶ Also of considerable interest are pre-nucleation clusters of oxide materials comprising metal cations coordinated by oxoanions, such as aluminum phosphate⁷ and zirconium/hafnium sulfate.⁸

In addition to studying pre-nucleation clusters to inform metal ion speciation in water, there is much motivation to investigate any persistent, discrete aqueous clusters that may exist under certain hydrolysis or dissolution conditions. These materials have found use in catalysis, in biochemical and biomedical applications, as precursors for materials, in water purification, in chemical surface polishing, as anticorrosion materials and in analytical chemistry.⁹⁻¹² Furthermore, the simple discovery of new cluster geometries and chemistries inspires us in their elegance and advances the field of inorganic synthesis. Pushing the boundaries of cluster size and shape as exemplified by two decades of fruitful exploration of giant molybdate clusters¹³ inspires synthetic pursuits and blends the borders between “molecular” and “nano”. Discovery of

new clusters typically begins with a solid-state single-crystal X-ray structure. Knowing the arrangement of the atoms is the single most powerful tool to explain structure-function relationships and drive the science forward to more discovery. However, a structure is not nearly enough to understand self-assembly processes and mechanisms of reactions that take place in water, and in the case of non-molecular clusters, determination of single-crystal X-ray structures is not possible. For these reasons solution characterization techniques, while more challenging to interpret unambiguously, are extremely important and provide considerable depth to our understanding of aqueous cluster chemistry.

The solid-state structures of clusters are very helpful in interpreting solution characterization. As a very straightforward example, ^{29}Si NMR spectroscopy might be used to determine if a Si-containing POM is stable in solution. To interpret the solution ^{29}Si NMR spectrum, we need to know how many Si-sites are present in the POM, and in what ratio, which is information readily obtained from the crystal structure. In the case of solid state NMR characterization, it affords additional opportunities for structural analysis. In the absence of molecular tumbling, interactions between nuclear spins and the surrounding environment can be evidence of local bonding, geometry, and morphology. The result is broad NMR resonances, which can yield structural details but can also be complicated by difficulties in deconvoluting complex overlapping features. Liquid phase NMR benefits from possessing very narrow resonances, where the frequency for resonance (isotropic chemical shift) indicates the species' chemical identity, and dynamics can be monitored.

Since the clusters of focus here are derived from water (and soluble in water) they are necessarily charged, they have counterions, and they can protonate or deprotonate in water. These characteristics drive their association and structures in water and can be studied by

methods covered in this **Perspective**. Furthermore, the single crystal structures provide information of the interaction between the charged clusters and their counterions, which cannot be ignored in understanding their solution speciation. Finally the single-crystal X-ray structure can provide opportunity to simulate spectroscopic data, in order to determine if the form and structuring of clusters in solution mimics what is observed in the solid-state. In addition, modern quantum mechanical computations have enabled additional insight on nanoscale clusters and their interactions in solution, which can greatly inform the interpretation of the analytical data.

In this Perspective we provide an overview of a variety of characterization techniques that inform the solution and solid-state characterization of clusters, and describe how the techniques complement and/or corroborate each other. Through case studies provided within each highlighted technique, several clusters will be discussed, including: Keggin $(\text{Al}_{13}\text{O}_4(\text{OH})_{24}(\text{H}_2\text{O})_{12})^{7+}$ (**k-Al₁₃**), flat- $[\text{M}_{13}(\text{OH})_{24}(\text{H}_2\text{O})_{24}]^{15+}$ (**f-M₁₃** where M = Al or Ga), uranyl peroxy-pyrophosphate $[(\text{UO}_2)_{24}(\text{O}_2)_{24}(\text{P}_2\text{O}_7)_{12}]^{48-}$, Lindqvist ions $(\text{H}_2[\text{Nb}_6\text{O}_{19}])^{6-}$, $\text{Hf}_4(\text{OH})_8(\text{OH}_2)_{16}^{8+}$, $\text{H}_{10}[\text{Nb}_6\text{P}_4\text{O}_{24}(\text{O}_2)_6]$ (**Nb₆**)¹⁴ and $\text{Bi}_6\text{O}_4(\text{OH})_4(\text{NO}_3)_6 \cdot \text{H}_2\text{O}$. The following techniques are highlighted, in order of: 2-dimensional NMR spectroscopic techniques, electrospray ionization-mass spectrometry (ESI-MS), solid-state NMR spectroscopy, small-angle X-ray scattering (SAXS), dynamic and phase-analysis light scattering (DLS and PALS), Raman spectroscopy, simulations and computational studies. Emphasis will be placed on highlighting the functional uses and limitations of each method.

2. TECHNIQUES IN NMR SPECTROSCOPY

Nuclear magnetic resonance spectroscopy (NMR) uses the quantum-mechanical properties of atomic nuclei in a magnetic field resonating at characteristic frequencies to ascertain how atoms within a molecule bond to one another, thus making it a powerful tool for structural analysis that

is on par with X-ray diffraction (XRD). Single-crystal XRD provides information about the measurable dimensions such as bond lengths and angles of molecules, but some structural information is more difficult to determine. NMR chemical shifts of nuclei due to properties including molecular geometry or effects related to the electronegativity of nearby atoms can be used to determine more detailed structural features of a molecule. Interactions such as J coupling and the nuclear Overhauser effect (NOE) can also provide information about the interactions between atoms near one another and through space, respectively, to piece together entire structures.¹⁵ NMR was first described 75 years ago and has been used extensively in organic chemistry for almost as long. However, it has gained substantial ground for analysis in inorganic chemistry as well once methods were developed for probing quadrupolar nuclei (nuclear spin quantum number, $I > 1/2$), including high magnetic fields and ultra-fast magic-angle spinning (MAS) NMR to overcome the inherently large linewidths of typical quadrupolar species.^{16,17} For instance, we have developed techniques to synthesize a variety of aqueous hydroxy-aquo M_{13} cations (e.g., Figure 1B) that have benefited from these NMR methods. Solution and solid-state NMR spectroscopy have been vital in providing information about the different local environments for each atom in the structure and demonstrating that the solution structure of these clusters is largely the same as their single crystal counterparts.^{18,19} NMR methods have also proven key for establishing the dynamics for reaction of these clusters, including ligand-exchange and isomerization rates.

Several related studies have employed ^{27}Al , $^{69/71}\text{Ga}$, and ^{17}O NMR spectroscopy to investigate the structural features of Keggin-structured Al_{13} and Ga_{13} oxy-hydroxy cations as well as other ionic cluster species both in the solid and solution states.²⁰⁻²⁸ While the quadrupolar nature of Al and Ga nuclei often hampers their observation due to a combination of rapid

relaxation and very large linewidths (see section 2.IV below), solid-state NMR (ssNMR) nevertheless has provided information on the local coordination environment of gallium sites and the coordination number of aluminum sites (e.g., tetrahedral vs. octahedral).^{29,30}

Table 1. Properties of atomic nuclei for NMR spectroscopy. Relative frequency calculated at 600 MHz (14T).

Nuclei	¹ H	¹⁷ O	²⁷ Al	⁶⁹ Ga	⁷¹ Ga	¹¹⁵ In	¹¹³ In
Abundance (%)	99.99	0.037	100	60.4	39.6	95.7	4.3
Spin	1/2	5/2	5/2	3/2	3/2	9/2	9/2
Relative Frequency (MHz)	600.0	75.3	156.6	144.0	183.6	132.0	132.0
Relative Sensitivity (vs. ¹ H)	1.00	1.1 x 10 ⁻⁵	0.21	0.004	0.057	0.33	0.0015
Magnetogyric ratio, γ (10 ⁷ rad T ⁻¹ s ⁻¹)	26.75	-3.63	6.97	6.70	8.18	5.90	5.89
Nuclear Quadrupolar Moment (Q/millibarn) ³¹		-25.58	146.6	171	107	759	770

NMR methods have long been used to follow reactions affecting the symmetric Keggin-structure ions, but recently, more advanced ssNMR methods have been used to study aluminum and gallium-based hydroxy-aquo cations (referred to earlier as “**f-Al₁₃**” and “**f-Ga₁₃**” and shown in detail in Figure 1B). From this we have gained information about the unique M(III) environments within these cations, and now apply solution (¹H) NMR and complementary computations to provide a window into the complex proton spectra of these clusters in solution.³² Thus solution ¹H NMR is a valuable technique that can complement ssNMR to inform aqueous cluster speciation even in wet, polar solvents where proton exchange with solvent does not always prevent NMR analysis.

The enormous range of NMR timescales, microseconds to seconds, makes this method particularly suited to detect the structural transitions affecting these clusters in both solid state and in solution. One expects an assortment of labilities even in a single multi-metal cluster. Using the Group 13 monomer ions as an example of the range, the rate of aquo ligand exchange at 298K of $[\text{Al}(\text{H}_2\text{O})_6]^{3+}$ is 1.3 s^{-1} ; that of $[\text{Ga}(\text{H}_2\text{O})_6]^{3+}$ is 420 s^{-1} and $[\text{In}(\text{H}_2\text{O})_6]^{3+}$ is $40,000 \text{ s}^{-1}$.³³ This wide range of timescales is also expected to be manifested at these metals when they are exposed at the surfaces of the Group 13 clusters. These differences have made peak analysis considerably challenging for **f-Al**₁₃ in comparison to its **f-Ga**₁₃ and heterometallic **f-Ga**_{13-x}**In**_x counterparts because the chemical shifts for peaks that would normally be time-averaged singlets are all observed, leading to spectra with complex splitting motifs.⁹ However, this complicating factor also enables NMR to investigate the kinetics of ligand-exchange reactions and other dynamic species in these clusters. The following sections provide more specific case studies of NMR spectroscopy applied to cluster characterization, beginning with a discussion of ¹H-NMR.

2.1 ¹H-NMR. While ¹H solution-phase NMR is among the most ubiquitous techniques used for structure characterization in chemistry, metal-hydroxo clusters have a unique set of challenges due to enormous, unexpected complexity of peaks present in the spectra. More specifically, the two tridecamers **f-Ga**₁₃ and **f-Ga**₇**In**₆ have identical symmetry and should present with the same number of proton signals. However, the spectra of **f-Ga**₁₃ is significantly more complex and contains more proton signals due to the slower rate of exchange of the capping water molecules with the solvent DMSO on the gallium compared to indium ions. Recent first-principles calculations and computational studies have addressed the complexity of these spectra

and assigned the peaks for each cluster. This work has led to a better understanding of the ranges and relative chemical shifts for different types of protons in the $f\text{-Ga}_{13-x}\text{In}_x$ series of clusters.³²

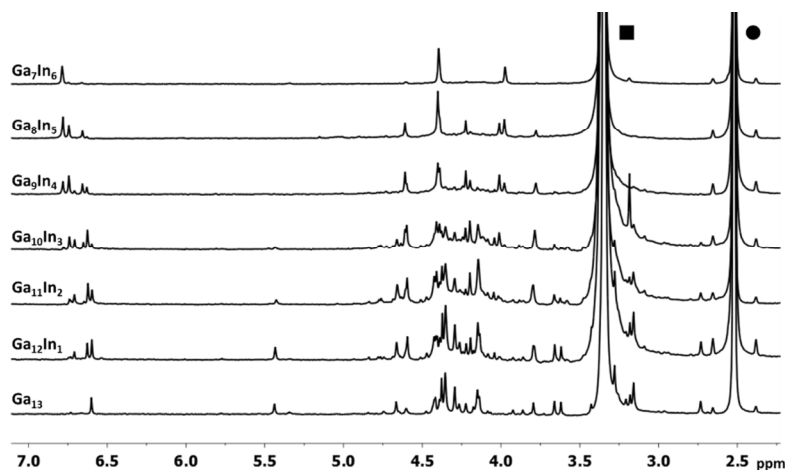


Figure 2. $^1\text{H-NMR}$ of 2 mM $f\text{-Ga}_{13}$ and each heterometallic $f\text{-Ga}_x\text{In}_{13-x}$ cluster in $d_6\text{-DMSO}$.

2.2 Diffusion NMR. In trying to decipher the NMR spectrum of a solution containing putative clusters, one is often left struggling to decide if the solution is truly monospecific, or if the various peaks are from different molecules, such as dissociation products or intermediates left over from formation of the cluster ion. Another technique used to characterize Group 13 polynuclear cations is diffusion NMR. Ideally the method can be used to assign experimental diffusion coefficients to different peaks in a spectrum and the Stokes-Einstein relation used to estimate the hydrated radius of the corresponding ion. This provides information regarding the size of these structures in solution, which is important in establishing the solution speciation of these clusters at different concentrations (a topic germane to the use of clusters as inks, as precursors for thin films or in polishing slurries).

In the simplest sense, the diffusion of a molecule in solution is a result of translational motion relative to the solvent caused by Brownian motion.⁹ This physical diffusion effects the dephasing of magnetism in the transverse plane and is detectable in certain NMR experiments.

From knowledge of the viscosity of solvent and the Stokes-Einstein equation: $D = (kT/6\pi\eta R_h)$, where k is the Boltzmann constant, T is temperature, η is solvent viscosity, and R_h is the hydrodynamic radius of the molecule,³⁴ one can estimate the molecule's diffusion coefficient (D) and size of the solvation sphere of a spherical species.

In this model D is inversely proportional to the hydrodynamic radius R_h , and thus molecules with larger radii have smaller diffusion coefficients. Therefore, 2D NMR diffusion experiments such as diffusion ordered spectroscopy (DOSY) can be used “to spectroscopically resolve” compounds based upon their transport properties in solution. DOSY maps chemical shift on the vertical axis against diffusion coefficient on the horizontal axis. Peaks with diffusion coefficients that pass through the same horizontal line are related to molecular species with the same hydrodynamic radius. As one example, in the case of a two-solvent (DMSO/DMF) experiment aimed at understanding **f-Al₁₃** speciation, the R_h for **f-Al₁₃** in DMSO-*d*₆ (0.97 nm ± 0.08 nm) and DMF-*d*₇ (0.68 nm ± 0.02 nm) are different owing to the change in solvent viscosity, η . Molecules in solvents with higher viscosity will move slower and thus have apparently larger R_h values (explained in greater detail later). Relative viscosity informs us that we expect R_h in DMSO-*d*₆ to be larger compared to that in DMF-*d*₇ (Table 2) even for the same cluster species.^{35,36}

Table 2. Ratio of the viscosities of DMSO-*d*₆ and DMF-*d*₇ relative to D₂O and H₂O at 25 °C.

	DMSO- <i>d</i> ₆ ^b	DMF- <i>d</i> ₇ ^c
D ₂ O ^a	1.818	0.732
H ₂ O ^a	2.227	0.897

^a Viscosity of D₂O and H₂O are 1.095 mPa·s and 0.894 mPa·s, respectively.

^b Viscosity of DMSO-*d*₆ is 1.991 mPa·s.

^c Viscosity of DMF-*d*₇ is 0.802 mPa·s.

An early example of identifying clusters in solution via $^1\text{H-NMR}$ spectroscopy was with 2 mM **f-Ga₁₃** in $\text{DMSO-}d_6$ (Figure 3).⁹ Additionally, it was revealed the slight differences between diffusion coefficients produced by the signals of the cluster can be ascribed to a number of factors including water exchange, overlapping of peaks, and/or data processing. The similarity in hydrated radius is evidence that the signals originate from a single cluster molecule, or at least from cluster molecules of similar sizes.

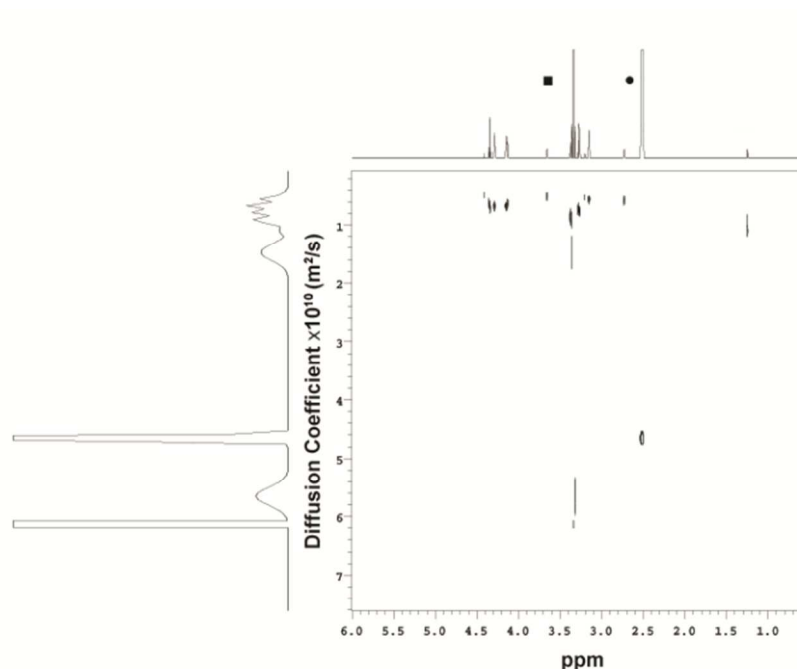


Figure 3. Representative DOSY spectrum of a hydrated **f-Ga₁₃** cluster in d_6 -DMSO ($D_{\text{avg}} = 0.955 \times 10^{-10} \pm 0.064 \times 10^{-10} \text{ m}^2/\text{s}$). (■) H_2O peak and (●) DMSO peak.

DOSY NMR is conceptually simple---the rates of transverse relaxation ($1/T_2$) are measured in a standard spin-echo experiment and then re-measured in the presence of a magnetic gradient. The difference in rates relates to the reorientation rate of the nucleus, and thus to diffusion coefficients. The most important parameters in our experience are the diffusion period (Δ), gradient pulse length (δ), and the gradient pulse strength ($G_{\text{max}}/\text{min}$). Smaller species like the **f-**

M_{13} clusters (ca. 1-2 nm diameter with ca. 70-80 non H atoms) require less time to move through the solvent compared to larger molecules such as proteins (ca. 10+ nm diameter), so the following values have worked well in our case: $50 \text{ ms} \leq \Delta \leq 100 \text{ ms}$, $2 \text{ } \mu\text{s} \leq \delta \leq 3 \text{ } \mu\text{s}$ and $G = 500\text{-}20000$.

G_{max} and G_{min} can change based upon the amount of attenuation necessary for reliable results and often depends on the particular sample, requiring optimization for specific clusters. Another issue that can arise in collecting DOSY data is when measurements are taken at non-ambient temperatures. Practically, not all spectrometer probes maintain a constant temperature well; therefore, a temperature gradient can exist within the sample. Since η will change with temperature it is important to minimize temperature variations within the sample. Using pulse programs with convection current compensations can help. In addition, loading the minimal amount of solution into the NMR tube required for a signal can also improve data quality.

2.3 Isotope-Exchange Dynamics: NMR and ESI-MS. Isotope-exchange has been used to study a variety of dynamic processes in cluster chemistry, such as ligand exchange and cluster-species interconversion using multinuclear NMR spectroscopy. These studies have established a set of not-inviolable rules for understanding some of the isotope exchanges, which we discuss below. As an example of reaction dynamics, ^{31}P -NMR spectroscopy on the very large uranium [U(VI)] molecule shown in Figure 4A revealed that this cluster exists in two equilibrating forms in solution: one an asymmetric dimpled structure that is stable at ambient conditions and the other a spherical form stable at slightly elevated temperatures. The molecule contains 24 uranyl (U) moieties, 12 pyrophosphate units³⁹ that are detectable via ^{31}P NMR, and a nominal stoichiometry of $[(\text{UO}_2)_{24}(\text{O}_2)_{24}(\text{P}_2\text{O}_7)_{12}]^{48-}$.

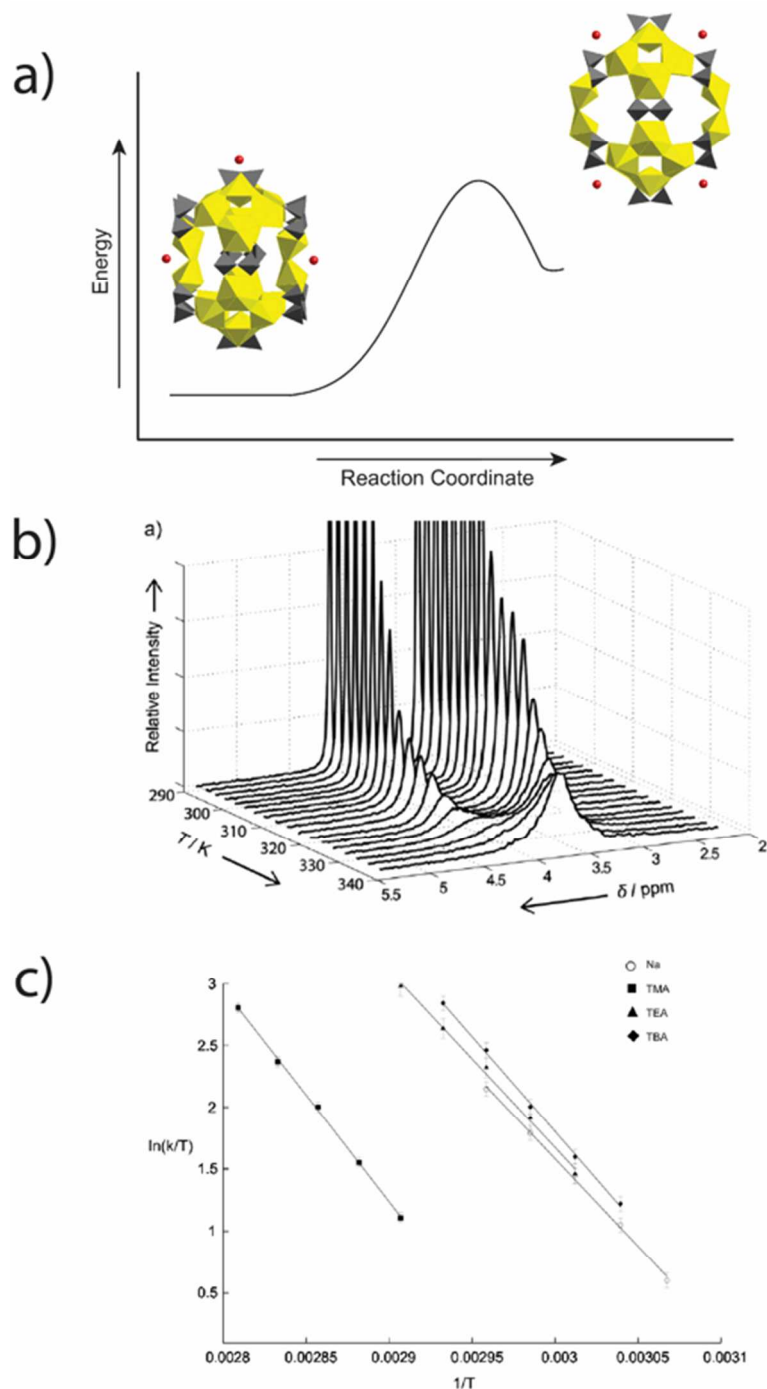


Figure 4. (a) A large uranyl-pyrophosphate cluster has two forms in aqueous solution. The two forms differ in the dimpling or symmetry and the nominal stoichiometry of the cluster is $[(\text{UO}_2)_{24}(\text{O}_2)_{24}(\text{P}_2\text{O}_7)_{12}]^{48-}$, excluding associated counterions. In the image, yellow are uranyl-oxide polyhedra, the gray tetrahedra are pyrophosphates and the spheres are sodium counterions. (b) ^{31}P -NMR spectra show the progressive coalescence of the two ^{31}P sites in the structure as the rates of isomerization increase with temperature; (c) the reaction rates are affected by the counterion chosen for the system. Tetramethylammonium ion selects for the asymmetric form. The system is an excellent example of two-site exchange in an NMR system, although in this case the two sites are within the same molecule and become magnetically equivalent as the structure isomerizes rapidly.

A surprising feature of this molecule is that the two isomeric forms can be caused to interconvert in second to millisecond time scales, and the rate depends on the temperature, pressure and the counterions present.⁴⁰ Interestingly, the asymmetric form is also made stable by increased pressure and by choice of tetramethylammonium as a counterion. This example illustrates the importance of solvation forces in affecting these large oxide ions in solution. High pressure selects for the more highly solvated species that provides a more efficient packing of water molecules. Because these clusters are often stabilized by solvation forces, the use of high pressure NMR may become an important tool in unraveling the chemistry that makes particular forms prevalent.

This example of the large uranium ion also illustrates the wider point that these large clusters are commonly equilibrating with metastable forms. For many dense clusters, these metastable forms control the rates of isotope exchanges into the structure from solution, the kinetics of dissociation of the clusters and, probably, the access to lacunary structures. Access to the intermediate forms involves concerted motions of much of the dense ion structure, which is why a single-metal substitution into a structure often has a mitigating effect on the kinetics of oxygen-isotope exchanges^{41,42} the substitution suppresses or enhances the stability of the metastable form. The NMR studies of oxygen-isotope-exchange pathways suggest a series of steps are common to these reactions: (i) a metastable structure forms from the partial detachment of a surface metal from an underlying over-bonded oxygen; (ii) this loose metastable structure allows water or oxygen solutes to add to the newly under-coordinated metal; (iii) protons transfer to basic oxygens in the metastable structure; and (iv) isotope shuffling occurs between relatively low-coordinated oxygens and, finally, (v) the metastable structure collapses into the stable form. The series of steps accounts for much of the observed data on rates of isotope exchanges in oxo

clusters like the niobate anions or aluminate cations. The rates of isotope substitution are regiospecific, are affected by choice of counterion, and yet the pH variation is similar for most oxygens in the structure, even though they may differ by orders of magnitude in reactivity. Counterions and solvation forces are important because charge separation is essential to forming the metastable structure.

The methods of following such reactions fall into two broad categories: (i) isotope-injection methods, and (ii) line-broadening methods. The most common methods of detecting oxygen-isotope exchanges in an injection experiment are NMR spectroscopy, vibrational spectroscopy and electrospray-ionization mass spectroscopy (ESI-MS). The last method has been reviewed recently for applications related to polyoxometalates by Ohlin⁴³ and there exist many good examples of the application.⁴⁴

The difficulties of ESI-MS lie in the ionization step where the cluster ion may fragment, may associate, or may pair with counterions so extensively as to yield uninterpretable spectra. Electrospray ionization depends upon controlled desolvation of a droplet after charge has been imparted at the injector into a stream of drying gas (commonly nitrogen at 300 °C or so). The ionization step requires a potential be placed between solution at the tip of the injector and the instrument. This potential is essential to forming a cone of dispersing solvent but the ionization potential can be a source of artifacts if it induces fragmentation or association of the cluster as well as the droplet. Maps of the m/z signals as a function of ionization potential can help detect misleading signals as the disappearance or appearance of signals as a function of potential. For instance, contoured plots of m/z values versus ionization cone voltages are extraordinarily useful in identifying cases where the cluster is affected by the electrospray process.^{43,44} In these plots, one can see clusters changing stoichiometry as a function of collision-induced dissociation or partial dissociation of a cluster. Changes in cone voltage can also induce redox reactions and changes in the effective pH of the solution.^{43,44} Choice of the solvent type also limits application of ESI-MS to cluster studies as, in general, volatile solvents (e.g., acetonitrile) and counterions (NH_4^+) are better than water and nonvolatile counterions (e.g., Na^+).

In the best of cases, the injection method can follow changes in the m/z value for key signals in the ESI-MS spectra. The magnitude of the shift not only shows the efficacy of isotopic substitution but if the stoichiometry of substitution is understood, it also allows one to assign charge to the fragment and to compare fitted and measured spectra. An excellent example is provided by Ohlin, et al. (2009)⁴⁵ who followed the ^{18}O substitution into a manganese-cubane oxide cluster and could resolve rate data into all four oxygens.

In other cases, and stemming from the earliest days of polyoxometalate chemistry^{22,46-48}, the ^{17}O -NMR signal in the structure is followed as a function of time. Most useful are cases where there remains an oxygen site that is inert to substitution so that the full dissociation of the molecule can be detected as exchange of isotopes with the solvent. For molecules like the MAI_{12} Keggin structures ($\text{M} = \text{Al(III)}$, Ga(III) or Ge(IV) ; $[\text{MO}_4\text{Al}_{12}(\text{OH})_{24}(\text{OH}_2)_{12}]^{7/8+}$), the μ_4 -oxo ligands in the center of the molecules are inert to substitution.^{49,50} In a typical injection experiment, ^{17}O is added to the solution and the evolution in signals followed by ^{17}O -NMR. An alternative approach is to synthesize the molecule from ^{17}O -enriched solvent, crystallize the product and dissolve it metathetically in isotopically normal water. This latter approach has been taken by many scientists studying inert-metal clusters, like niobates.⁵¹⁻⁵² The injection methods are simple and differ only in how the isotopic substitution is detected. In a similar manner, vibrational spectroscopy techniques can be used to complement these other two techniques.

The timescale for reaction dynamics in many large clusters fall into the 10^{-9} - 10^{-2} s range, which makes the detection amenable to NMR if there exists a suitable nucleus. The NMR methods used to follow the exchange of isotopes or movement of mass into, and out of, the cluster are dominated by line-broadening approaches,⁵³⁻⁵⁶ although there is no reason that

selective-excitation methods cannot also be used. Application simply awaits a polyoxometalate system with appropriately spaced resonances and suitable kinetics of exchange.

The essence of the line-broadening methods is progressive coalescence of NMR signals with rates of substitution enhanced by temperature or pressure. Even for cases where only a single resonance is followed, such as ^1H -NMR studies of exchange in polyoxometalate ions, implicit in the approach is that the spectra change shape as rates of exchange increase between two sites—one site is the solvent which is largely unaffected, the other site is the proton on a structural oxygen on the polyoxometalate ion. The assumption of two-site exchange is almost invariably invoked because oxygens or protons in the solvent are in such high excess that the change of three-site or multi-site exchange, such as collisions between cluster ions that lead to an exchange event, are highly improbable.

^{17}O -line broadening studies fall into two categories: (i) cases where changes in the peak assignable to the solvent are followed, and (ii) cases where peaks assignable to the solute are followed. The former case is particularly important for solutes of paramagnetic metals in rapid-exchange with bulk waters because the NMR signal for ^{17}O bound to the paramagnetic metal is invisible. The reaction kinetics are inferred from the peak shape for the solvent. This subject, and its assumptions, was recently reviewed.⁵⁷

The second case, where distinct and well-separated NMR signals assignable to nuclei in the cluster are followed, has two subcases. The first, typified by studies of ^1H -NMR and line broadening, is where one exchanging site is in large excess over the site in the solute, here a cluster ion. In this case the contribution to transverse relaxation and linewidth (via $1/T_2$) from chemical exchange must be larger than from all other sources. If this condition is met, then the rate of exchange is directly proportional to the full-width-at-half-maximum of the solute peak.

Ideally, one can simply estimate the rates from the full-width-at-half-maximum of the NMR peak. This approach was used by Houston, et al. for the $\mathbf{k-AlI_3}$ ion.⁵⁸ Simulations of the Bloch-McConnell equations for NMR line shape, followed by fitting of the approximate equations, shows that this assumption is generally good to a factor of ~ 2 in values of k_{ex} at their conditions. The validity of the assumption depends upon the ratio of exchangeable nuclei in the two sites, the separation of the NMR peaks in Hz, and the rates of exchange. This assumption should be tested for each case.

The second case is exemplified by Figure 3B, where the ^{31}P -NMR signals for this nanometer-sized cluster coalesce with increased temperature. This case also represents a two-site exchange problem, but the two sites are within a single molecule undergoing a reversible isomerization reaction. The two sites broaden with temperature, move together and establish a characteristic exchanging line shape before coalescing into a single peak and becoming increasingly narrow as temperature increases. The two sites are becoming magnetically equivalent because of the rapid interconversion of the large oxo ion and establishment of higher symmetry. The asymmetric and symmetric forms interconvert at rates faster than the separation of the ^{31}P -NMR signals from the two sites (Figure 3C). Deriving rate coefficients from such a case requires a numerical fit to the Bloch-McConnell equations, which was impossible decades ago when approximate solutions were derived and used. Now computers are so fast that the full equations can be solved directly and repeatedly using a nonlinear-least squares algorithm and the rate coefficients derived without approximation (see Equations 1-3, in footnotes).[†]

2.4 Solid-state NMR (ssNMR). Quadrupolar solid-state nuclear magnetic resonance (ssNMR) spectroscopy has received increased interest with recent advancements of ultra-high magnetic fields and very fast magic-angle spinning (MAS) NMR probes. With these advancements,

ssNMR offers a unique modality for the characterization of molecular clusters for multiple reasons. First, amorphous domains, disorder, and impurities present in samples are often still observable by NMR, unlike X-ray diffraction (XRD) which is generally unable to discern these due to the lack of long-range order. ssNMR is both element-selective and a quantitative spectroscopic technique where the NMR resonances can be recorded such that the signal is proportional to the number and type of sites present for the isotope being probed in the material.⁵⁸ ssNMR is also a nondestructive technique, where the integrity of the sample remains intact after analysis, allowing other characterization techniques to be employed on the identical sample.

The most familiar experiments performed with NMR involve nuclei with nuclear spin quantum numbers $I = 1/2$, such as ^1H and ^{13}C . However, the vast majority of the periodic table contains quadrupolar nuclei, i.e. spin $I > 1/2$. One such quadrupolar species is gallium which was widely used to explore semiconductor materials since the late 1950's,⁶⁰ and has recently been applied to other materials.^{5,61,62} Gallium has two NMR active isotopes, ^{69}Ga and ^{71}Ga , which are quadrupolar, and both have spin $I = 3/2$. While ^{69}Ga is more naturally abundant at 60.4% compared to ^{71}Ga at 39.6%, its quadrupole moment is approximately twice as large as ^{71}Ga which results in much broader NMR resonances. ^{69}Ga is useful to confirm spectroscopic assignments, but ^{71}Ga is typically the isotope of choice to acquire and model NMR spectra.

We have reported the synthesis of a family of **f-M₁₃** clusters, including the gallium hydroxo-aquo cluster, $[\text{Ga}_{13}(\mu_3\text{-OH})_6(\mu_2\text{-OH})_{18}(\text{H}_2\text{O})_{24}](\text{NO}_3)_{15}$ (**f-Ga₁₃**, Figure 1B),^{5,62} and we recently reported its solid-state NMR characterization. These spectra revealed three gallium sites (Figure 5): a core, a middle ring, and an outer ring site were each present.⁶³ These molecular clusters present a unique challenge for solid-state NMR due to the local environments that lead to

significant broadening of the resonances. However, the three types of sites could be resolved by utilizing multiple magnetic fields and modelling of the Ga_{13} structure. Herein, we present a brief overview of how ssNMR can be used to investigate the gallium coordination environment in solid materials.

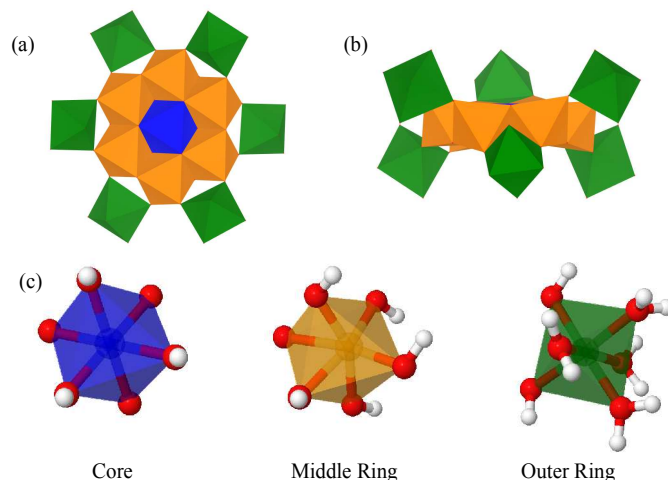


Figure 5. Space filling polyhedral representation of the Ga_{13} molecular cluster from a geometry-optimized calculation (a) top down view, (b) side view, (c) individual polyhedral representation of the three gallium sites: core (blue), middle ring (orange), and outer ring (green).

The three types of coordination environments observed in the Ga_{13} cluster all consist of six-coordinate gallium atoms: an outer ring of six gallium sites, a middle ring of six gallium sites, and one site in the center. Each site is in a distorted octahedral environment¹⁸ and a detailed table of bond angles and lengths is provided in the supplemental information. The ability of ssNMR to resolve the three coordination environments required the use of two magnetic fields (13.9T and 21.1T) for full characterization due to second-order quadrupolar broadening effects for some sites (which are reduced at higher magnetic fields).^{59,18} At lower field, 13.9T, the core and outer ring sites were the most prominent, while the middle ring remains broadened into the baseline and was not well resolved (Figure 6a). However, by obtaining the data at higher field (21.1T, Figure 6b), all three sites were fully resolved. A small resonance assigned to an impurity left

over from the synthesis, which has been identified as gallium nitrate, is denoted by the double dagger.

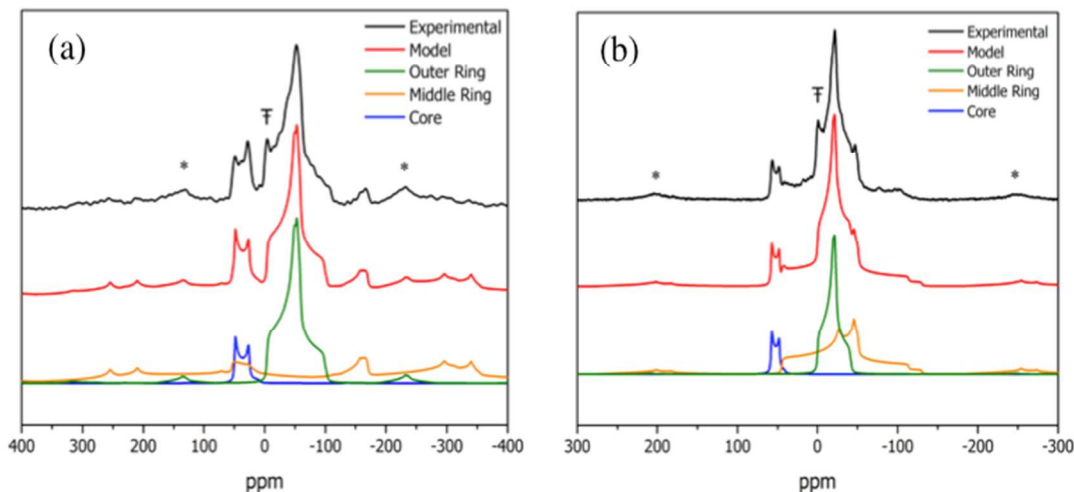


Figure 6. ^{71}Ga MAS NMR spectral data for the Ga_{13} molecular cluster at two magnetic fields, (a) 13.9T and (b) 21.1T. Experimental spectra data are shown in black, the individual line shapes are shown in blue (core), orange (middle ring), and green (outer ring), and the red spectrum is the compiled model. Asterisks denote spinning side bands of the central transition, and the double dagger indicates the position of the gallium nitrate impurity resonance.

The quadrupolar parameters give insight into the local structure surrounding each gallium. Since ^{69}Ga and ^{71}Ga isotopes both possess a non-zero quadrupole moment, this quadrupole moment may interact with the electric field gradient (EFG) surrounding each nucleus (Figure 7). The EFG is composed of three principal tensor components, V_{xx} , V_{yy} , and V_{zz} , where $|V_{zz}| \geq |V_{xx}| \geq |V_{yy}|$, when diagonalized in the principle axis system.⁶⁵ The orientation and size of the ellipsoids in Figure 7 are defined by these principal tensor components. The size and shape of the EFG lead to parameters that aid in the interpretation of the data. The first parameter is the axial asymmetry parameter, η_Q , which is strongly reflected in the shape of the resonance, and the second parameter is the quadrupolar coupling constant, C_Q , for simplicity it can be defined as the breadth of the resonance. By using the principal tensor components, the axial asymmetry parameter may be calculated from the following equation (1):

$$\eta_q = \frac{V_{yy} - V_{xx}}{V_{zz}} \quad (1)$$

where $0 \leq \eta_Q \leq 1$. The quadrupolar coupling constant C_Q (in hertz) is defined by the following equation (2):

$$C_Q = \frac{e^2 q Q}{h} \quad (2)$$

where eq is V_{zz} , eQ is the nuclear quadrupole moment, and h is Planck's constant. Combining these two parameters, the NMR line shapes defined by these two will give insight into the local bonding of the cluster. Utilizing first principles calculations (CASTEP code),⁶⁶ it was possible to calculate the electric field gradients in a complex system such as this molecular cluster and estimate the quadrupolar parameters η_Q and C_Q . The parameters were then used in conjunction with simulation software (DMFIT⁶⁴), which allows for lineshapes to be simulated based on specific quadrupolar parameters and compared to the experimental data. These values were adjusted to obtain a good match between model and experiment. The size of the electric field gradients provide insight into bond lengths and bond angles, as well as other atoms in the vicinity of each quadrupolar nucleus. In addition to the directly bonded structure, the electric field gradients can be strongly affected by the counterions (nitrates) present around the cluster and can cause significant distortions to the EFGs. In the Ga_{13} clusters, the largest quadrupolar coupling constant was observed in the middle ring sites (the largest grey spheres), and the smallest C_Q was the core site (barely visible on this scale). While the outer ring contains a fairly large C_Q , it remained significantly smaller than that of the middle ring.

The core site of the Ga_{13} structure had the most axially symmetric environment, meaning that there was little distortion in the EFG $\eta_Q \approx 0$ (Figure 6). An axially asymmetric site will contain large distortions to the electric field gradient, i.e. the grey ellipsoids are large in two dimensions,

but compressed in one dimension, which yields an $\eta_Q \approx 1$. This type of axially asymmetric site was observed in the middle and outer ring of the Ga_{13} molecular structure.

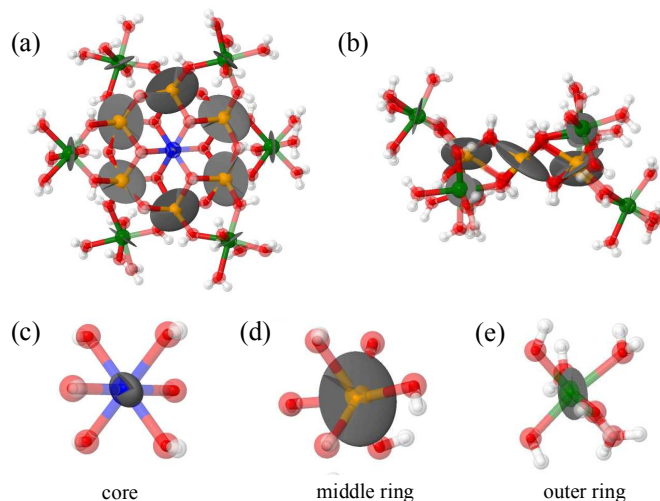


Figure 7. A geometry-optimized structure of the Ga_{13} molecular structure computed from CASTEP (a) top view and (b) side view. The electric field gradient depicted as distorted grey shapes (ellipsoids) around the gallium atoms. The core gallium, which is highly symmetric, has a small EFG, which is difficult to see in this rendering. The individual sites have been extracted to depict the electric field gradients surrounding each atom: (c) the core site, (d) middle ring, and (e) outer ring. The core EFG in figure 3c was multiplied by a factor of 2.

Solid-state NMR has provided structure characterization of each of the Ga^{3+} sites in the molecular cluster. Utilizing multiple fields allows for the sites to be assigned and validated by NMR simulations. The quadrupolar parameters, η_Q and C_Q , give insight into the local environment of the gallium sites. First principle calculations offer a starting point for interpretation of the experimentally-measured data, and here these calculations were utilized to compute the electric field gradients around each nucleus. While very high magnetic fields and high-speed magic-angle spinning are required for analysis of such broad NMR resonances (of such quadrupolar species), the ability to observe (and potentially quantify) impurities is an invaluable aspect of the technique. Another advantage of ssNMR is that disordered materials and amorphous domains can still be probed by this form of spectroscopy. We can add a cautionary note that disorder in these M_{13} systems is sufficient to cause distortions to the EFG's (like those

shown in Figure 7) in the Al_{13} system, such that similar analyses on Al_{13} have failed to yield just 3 sites (data not shown).

3. SCATTERING TECHNIQUES IN AQUEOUS CLUSTER CHEMISTRY

3.1 Studying clusters via SAXS. During a SAXS experiment, a sample is irradiated by a collimated, monochromatic beam of X-rays. The particles in solution scatter the X-rays while the intensity of this scattering is collected by a detector. SAXS exhibits coherent, elastic scattering where the electrons in the irradiated particles oscillate at the same frequency as the incoming X-rays, and emits X-rays with the same wavelength as the incident beam. The coherent X-rays will then interfere with one another either constructively or destructively creating interference patterns that provide structural information about the clusters.⁶⁷

A scattering measurement is composed of an isotropic average of scattering signals from all particles in all orientations relative to one another. The overall scattering of a solution is the contrast in electron densities between particles of interest and the solvent. X-rays are also scattered by solvent molecules, so data processing is necessary to subtract out bulk solvent as a background and scale relative intensities. More intense scattering is the result of larger differences in electron densities between solute and solvent. For this reason, clusters provide the optimal scenario for SAXS studies since they are composed of high Z metals with solvents of low Z elements (Z = atomic number). The discrete, monodisperse nature of polyoxometalates and Group 13 polycationic clusters (under most conditions) makes them ideal species to study in solutions with SAXS.⁶⁸ We can also utilize SAXS to observe polydisperse species such as pre-nucleation clusters mentioned previously. Even though a polydisperse system can be identified from scattering measurements, it is not an ideal method for extensive characterization.

Monodisperse species are more ideal for SAXS as they can be used as model systems to understand related polydisperse mixtures.

When interpreting SAXS data, one dimensional data is used to extract information about a three dimensional particle. There are a number of mathematical formulae that are derived from scattering contrast, size and shape of particles, and interaction between particles. Some formulae are used for specific regions of the scattering curve such as the Guinier (low q) and Porod (high q) methods; and others are for whole curve fitting, such as the Fourier transform method of Moore.⁶⁷ Thus arriving at the same description of scattering species from multiple methods is optimal, since there is not always one unique solution for every data set. Therefore, reaching the same conclusion by two or more curve-fitting routines lends robustness to the interpretation.

Scattering data on solutions of clusters is often described by a radius of gyration (R_g). R_g is a shape independent root mean square measure of all mass weighted vectors in the particle from the center of mass.^{67,69} The size distribution of particles can also be determined, along with particle shape including spherical, disc-shaped, and cylindrical. Scattering data is dependent on form factors (size, shape, and scattering contrast) and structure factors (interactions between particles).⁷⁰ Another often-used data treatment is the pair distance distribution function (PDDF) from Moore's Fourier transform method.⁷¹ This method transforms the reciprocal space data to real space and yields a geometrical representation of the scattering particle as a probability histogram ($p(r)$ vs. radius). In this representation, the radius is distance from the edge of the particle to any other point within the particle. Therefore the number of equivalent length vectors within the particle is represented as a probability. The shape of the PDDF can give some initial information as to the shape and size of the scattering particle. Where $p(r)$ goes to zero is the

maximum linear extent, or roughly the diameter of the scattering species. Figure 8 illustrates a variety of PDDFs for different geometric shapes of scattering particles.

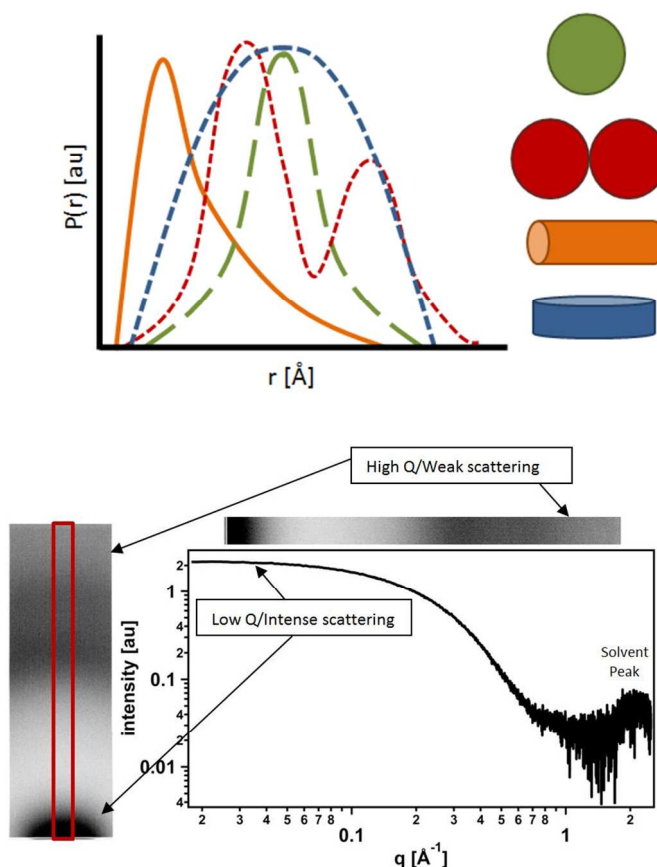


Figure 8. One dimensional data extracted from a two dimensional scattering pattern. (left) Pair distance distribution functions indicative of particle shape (right).

We are particularly interested in using SAXS to investigate the process of conversion of 1) discrete metal-oxo clusters in solution to 2) macromolecules or inorganic polymers to 3) extended solid-state materials. These reactions usually are initiated or occur by electrostatic association (i.e., cation-anion association) or formation of covalent bonds, such as by hydrolysis and condensation reactions. The first two states listed above can be monitored by SAXS when species still remain soluble, but the eventual conversion to a solid can be investigated by other X-ray methods such as PDF (pair distribution function). Three case studies are reviewed below:

- 1) Forming LiNbO_3 thin films with optimal morphology, density and phase purity by taking

advantage of H-bonding between clusters in solution.⁷² 2) Understanding the mechanism of linking clusters in solution (formation of macromolecular chains) by varying aqueous conditions.⁷³ 3) Investigating the polymerization of Hf-tetrameric clusters with sulfate anions in solution *en route* to gelation of hafnium sulfate coatings for nanolithography.⁷⁴ All three studies utilize the solid-state structure of discrete clusters, with or without their counterions, to derive reasonable models for complex solution behavior of interacting and reacting clusters.

1.3.1.1 Lithium niobate thin films from cluster precursors. Previous studies on decavanadate have surmised that crystallization of the clusters in a lattice occurs through mutual hydrogen bonding of the protonated faces, and that this protonation is solvent dependent.^{75,76} Many diprotonated Lindqvist ions ($\text{H}_2[\text{Nb}_6\text{O}_{19}]^{6-}$) (Figure 9) have been structurally characterized in the solid state and have been observed to associate as mutually H-bonded dimers in the crystalline lattice.⁷⁶

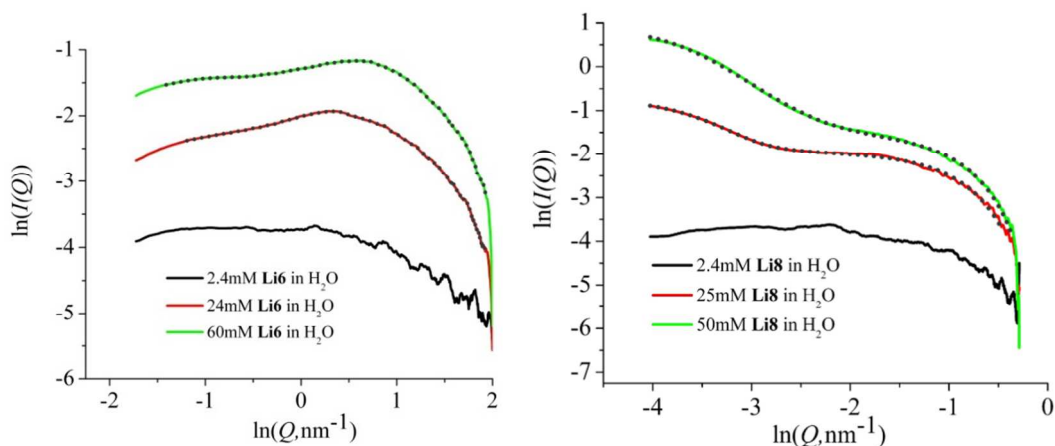


Figure 9. SAXS scattering curves for Li_6 (left) and Li_8 (right) along with a total curve fit (dotted line) for the highest concentration. For Li_6 , the curves feature a broad peak around $\ln(q)=1 \text{ nm}^{-1}$, which indicates interactions between clusters. The Li_8 curves were fit with two-phase models, where the phase of larger scattering species (curve fit between $\ln(q) = -4$ to -3 nm^{-1}) indicates incipient crystallization of the clusters.

This has inspired the investigation of their dimerization behavior in solution using SAXS. By exploiting the protonation behavior of hexaniobate, we can convert $\text{Li}_8[\text{Nb}_6\text{O}_{19}]$ (Li_8) to $\text{Li}_6\text{H}_2[\text{Nb}_6\text{O}_{19}]$ (Li_6) for use as a precursor for LiNbO_3 thin films.⁷² This simple acidification of

the cluster led to improved solubility behavior and better thin film quality in addition to providing the correct Li:Nb ratio for the targeted perovskite material. SAXS studies were used to gain insight into the differences between the Li_8 and Li_6 in solution. At low concentrations, both clusters in solution have R_g 's that agree with an unassociated Lindqvist ion; however, high quality films are deposited at higher precursor concentrations and, therefore, these conditions provide more relevant insight to the processes leading to film formation.

In the Li_8 solutions pre-nucleation aggregates form and begin to crystallize. This was observed in changes to the slope in the low- q region of the scattering curve (Figure 9). The aggregation varies with cluster concentration: at lower concentrations there are larger, less abundant aggregates, while the opposite is true for higher concentrations, consistent with incipient crystallization of a solution. For Li_6 solutions, the PDDF suggests dimerization as we would expect for a protonated cluster. Moreover, association between the dimers in solution was observed in solution, as indicated by a broad coulombic peak in the scattering curve (Figure 9).

The morphology observed in the thin films from Li_6 and Li_8 indicate gelation of the dissolved species with increased concentration, and crystallization of the dissolved species of the substrate, respectively. This is consistent with crystallization behavior of these clusters.

3.1.2 Understanding the mechanism of linking clusters in solution. Since the first reported dodecaniobate Keggin structure⁷⁷ of $[\text{XNb}_{12}\text{O}_{40}]^{16-}$ ($\text{X} = \text{Si}, \text{Ge}$; see Figure 1 for illustration of Keggin ion), these clusters have been observed to link into infinite anionic chains,⁷⁸⁻⁸⁰ where the linker is a dimer of edge sharing octahedra (MO_6). A monomeric building block of these chains, (as well as a dimer) have been isolated as $[(\text{Nb}=\text{O})\text{GeNb}_{12}\text{O}_{40}]^{13-}$ and $[(\text{Nb}-\text{OH})\text{GeNb}_{12}\text{O}_{40}]_2^{24-}$. Through the structure of the dimer, evidence suggested that the protonation of the $\text{Nb}=\text{O}$ cap to

form Nb—OH is key to promoting polymerization. SAXS was used to study the effect of the counterion and protonation on this polymerization.

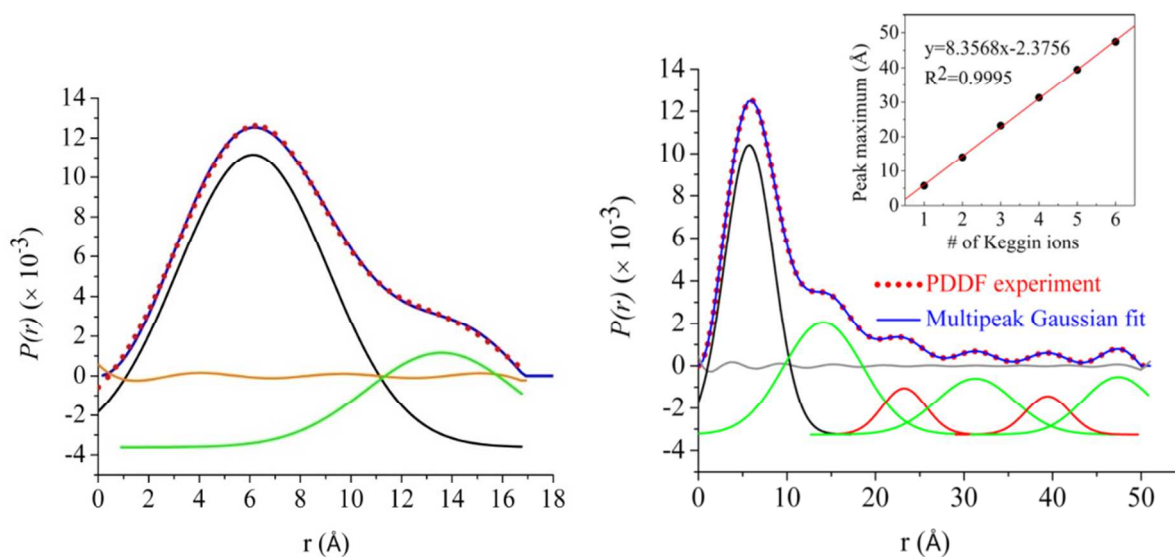


Figure 10. PDDF analysis of Cs (left) and Rb salts (right) of dodecaniobate $[(\text{Nb}=\text{O})\text{GeNb}_{12}\text{O}_{40}]^{13-}$. Black peak is the monomeric unit, green peaks are long axis of dimers, red dots are experimental data, and blue is the multipeak Gaussian fit.⁷⁵

Two different aqueous conditions were used to create one environment where protonation prevailed and one where it was inhibited. In TMAOH solutions, Cs and Rb salts of the clusters did not protonate and no polymerization was observed. SAXS data suggested solutions of discrete, monodisperse species whose size (as determined by PDDF and Guinier analysis) was representative of the capped Keggin ion. In neat water, the clusters protonate and provide a self-buffering pH of ~ 10 -11. The Cs salt in water revealed mostly monomers and dimers. In the Rb salt solutions, extensive polymerization occurred with a mixture of chain lengths featuring up to six Keggin ions (figure 10).

PDDF is a valuable tool in identifying polymerization as multiple, distinct peaks are observed for each additional linkage. This difference in polymerization between Cs and Rb salts can be explained through ion association. Cs provides stronger ion association than Rb. Therefore, less protonation occurs on the cluster and thus less polymerization.⁷⁵

3.1.3 Investigating the polymerization of Hf-tetrameric clusters with sulfate anions.

Stemming from another thin film study aimed at developing inorganic photoresists, hafnium sulfate clusters were studied in solution to gain insight into pre-nucleation and solution speciation.^{12,73,81} By understanding solution speciation and the solution behavior that yields dense smooth films, we can develop design rules for guiding the synthesis of new materials. Early X-ray scattering studies concluded that tetrameric species dominate in solutions of hafnium oxyhalides, which is consistent with the solid state structure.^{82,83} In a more recent study, hafnium sulfate solutions were observed using SAXS. As the solutions age, the average particle size increases significantly. It was found that the data could not be modelled by assuming simple spherical particles, and instead a cylindrical model was more adequate. The length of the cylinder was in good agreement with the maximum linear extent of the PDDF (providing an example of multiple mathematical routes to comparable interpretation), while the radius of the cylinder agreed with the size of the Hf-tetramer (Figure 1). A cylinder or rod is the appropriate model for this system because the tetramers are linking into chains. This is evident in the PDDF with periodic changes in the electron density. The extent of oligomerization depends on age and concentration of solution (Figure 11).⁷⁶

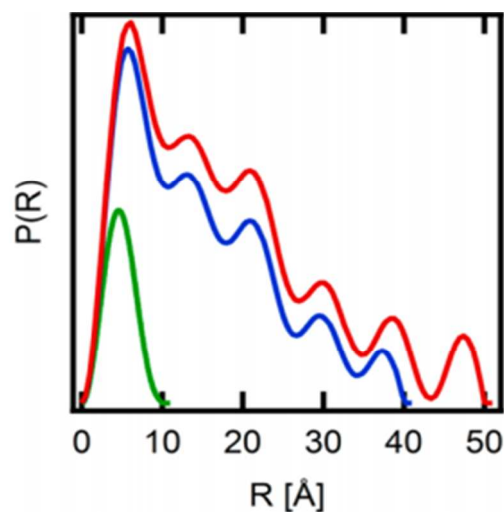


Figure 11. PDDF for 500 mM hafnium sulfate solution aged for 0h (green), 24h (blue), and 72h (red).⁷⁶

The major conclusion drawn from this study was that the robust Hf cationic tetramers remain the major building block of the Hf sulfate thin films, despite the fact that they are joined in multiple directions by sulfate anions. The presence of a uniform repeat unit in the form of a discrete cluster is likely the primary reason for the very smooth films and high resolution nanopatterning provided by these precursor solutions.⁸¹ The primary difference between the Hf-sulfate speciation and the previously described polyoxoniobates is the niobate clusters are limited by the linking chemistry under the mild conditions of the experiments. On the other hand, there are many sites at which the Hf tetramers can link (i.e., corner-to-corner, edge-to-edge and face-to-face) in addition to forming sulfato bridges. Therefore, it is more challenging to obtain a unique model for scattering data. In this event, it is valuable to model SAXS data from solid-state structures as well.

Finally, SAXS data can be simulated using the program SolX^{84,85} where a solid-state model is developed from single-crystal data files to create a scattering curve, which also fits models to the simulated data. Both the shape of the scattering curve and the PDDF profile should match the experimental data if the data interpretation is correct. R_g data can also be readily obtained, however, the absolute value needs to be considered carefully, as it is very sensitive to the definition of the radius of the atoms that make up the scattering species (i.e. ionic vs. atomic radius). These radii, however, can be optimized iteratively as many scattering data are obtained a variety of clusters featuring different metal cations.

3.2 Dynamic light scattering applied to cluster characterization. DLS is widely recognized as one of the most popular techniques for size measurements of nanoparticles, proteins, colloidal species, polymers, and more recently clusters in solution.^{63,86,87} More so, advancements in DLS

have allowed for relatively facile and routine detection of species as small as ~ 1 nm and lower in radius [R_h of 0.1 M $\text{Al}(\text{NO}_3)_3 = 0.35 \text{ nm} \pm 0.11 \text{ nm}$]. Some of the biggest strengths of this technique are that it requires a small sample volume (vol. $> 50 \mu\text{M}$), data collection can be performed within a matter of seconds, and it is non-destructive (except for light-sensitive materials). Additionally, depending on how well a given sample can scatter light, accurate measurements can be made in very dilute concentrations (sub- μM).⁸⁸ Experimentally, DLS has a wide array of applications including rapid screening of potential target materials, determining relative particle distributions of species in solution, prediction of optimal crystallization conditions, monitoring solution stability and rates of agglomeration/condensation, and determining temperature dependence of solution speciation. DLS is best used as a qualitative complementary or corroboratory piece to other techniques such as transmission electron microscopy (TEM), static light scattering (SLS), SAXS, Raman, and NMR.

While DLS is a fast and simple technique to utilize, it does carry some significant limitations in analyzing clusters in solution. Due to its inherent sensitivity and bias towards detecting larger particles or agglomerates, consistent detection of sub-5 nm species can become quite problematic if that species is unstable in solution (i.e. non-molecular clusters), or if there are larger aggregates in equilibrium at dilute concentrations with the smaller species of interest. DLS is also not particularly accurate in discerning multiple size distributions and the data may not be as reliable if there is no precedent available to calibrate a particular sample. Additionally, since DLS is sensitive towards detecting larger particles, if the solvent is contaminated or has bubbles present, any data collected could be adversely compromised.

DLS takes advantage of the fact that in solution, any cluster present is generally perturbed to some extent by the solvent in which it is dissolved, suspended, or solvated. This disturbance

between the cluster being studied and solvent results in the random motion of molecules in solution, or Brownian motion.^{9,89} As light scatters from the moving cluster, it imparts a random change to the phase of the scattered light, such that when the scattered light from two or more particles are added together, there will be a continuum of destructive or constructive interference as a function of time. These fluctuations in light intensity over time are converted into an autocorrelation function, in which a direct measurement of the rate at which a particle diffuses through the medium (the diffusion coefficient, D_t) is made. Typically, particles and agglomerates with larger radii will diffuse slowly while small particles diffuse more quickly. However, there are many other factors that can affect the measured value of a diffusion coefficient. Intrinsic factors that can alter diffusion rates include asphericity and inter-particle drag due to solvent-solute interactions, while extrinsic factors like solvent viscosity, cluster concentration, and temperature can play significant roles as well. It should be noted that the mass of a given particle has virtually no influence on the rate of particle diffusion, and may safely be ignored. And as stated in the earlier DOSY NMR section, an effective hydrodynamic radius (R_h) can be similarly calculated via the Einstein-Stokes equation.

3.2.1 Screening for clusters in solution. As a first case study, routine measurements of the following clusters in 500 mM aqueous solution were performed (viscosity effects were negligible): $H_{10}[Nb_6P_4O_{24}(O_2)_6]$ (**Nb₆**),¹⁴ $Hf_4(OH)_8(OH_2)_{16}^{8+}$, (**Haf(SO_x)**),⁷⁴ and $[Al_{13}(OH)_{24}(H_2O)_{24}]^{15+}$ (**f-Al₁₃**).⁶³ As expected, analysis revealed that upon immediate dissolution each cluster is approximately ~1 nm in radius and shows strong evidence towards being a discrete, monodisperse species in solution, as suggested by the narrow size distribution of each particle (polydispersity index% or PDI% < 15%). Furthermore, it is clear that each

cluster exhibits strikingly different size distributions than the starting material from which each was synthesized.

It should be emphasized that one cannot reasonably differentiate one discrete species from another using DLS since i) each cluster is fit as a spherical molecule, and ii) the error of propagation from the aforementioned factors such as cluster asphericity and cluster-solvent interactions are directly linked to the size measurement. As such, one should not rely on DLS alone as a definitive method for identifying new or unknown clusters in solution as many particles will ultimately have similar diffusion rates. However, it does serve well as a rapid screening technique to identify possible positive leads for identifying clusters in solution.

3.2.2 Monitoring the solution stability of aqueous hafnium sulphate clusters. One of the most practical applications of DLS in cluster analysis is the ability to consistently monitor rates of cluster aggregation or dissociation as a function of time. Figure 12 shows a three day study of 500 mM **HafSO_x** with and without the addition of H₂O₂ as discussed in the previous SAXS section.^{73,81}

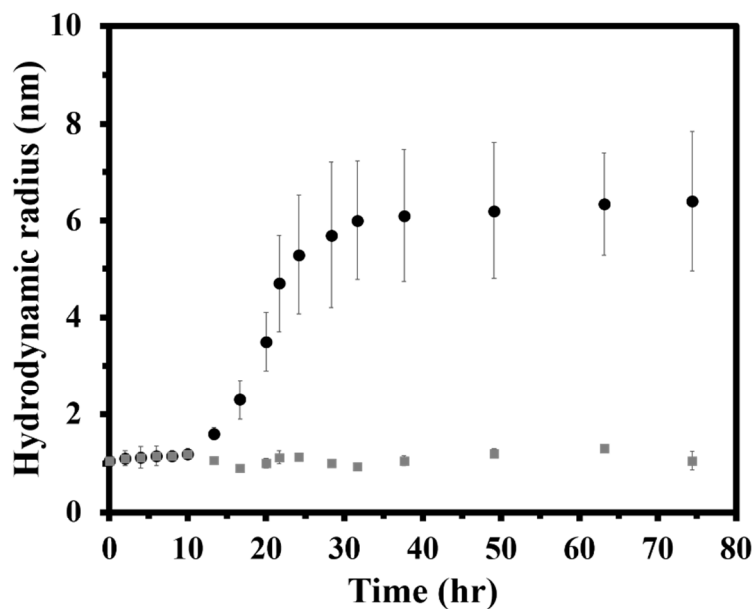


Figure 12. Time stability study of 500 mM hafnium sulphate (HafSO_x) with added H₂O₂ (grey) and without H₂O₂ (black). The large error that is prominent at the later times is due to a high degree of polydispersity that is inherent with HafSO_x over time.

After a period of ~24 hours, the **HafSO_x** solution without peroxide grows to nearly 4x its original size of 1 nm and agrees well with the **HafSO_x** PDDF experiment described earlier (Figure 10 in SAXS section). Over several days the rate of decomposition eventually slows down to reach a high point of approximately 6.3 nm ± 2.7 nm as the solution began to crystallize. However, it should be again noted that unlike SAXS, DLS gives no information about the molecular shape of the nano-agglomerate that forms and thus the large error associated with the increase in particle distribution increases (i.e. increase in polydispersity) is due to the asphericity of the **HafSO_x** agglomerate. Ultimately, DLS is very valuable for determining kinetics qualitatively but can become ambiguous to analyze and quantify such rates if the system is non-ideal or supporting evidence is lacking.

Lastly, we will discuss the importance that concentration, particular high concentrations, can play on data collection and interpretation. Many factors must be taken into account when

working with high cluster concentrations (Molarity > 1 M), including: electrostatic interactions, viscosity changes due to the solute, and multiple scattering species. However, some of these concentration effects can be accounted and compensated for by using equation 3:^{89,90}

$$D_t = D_0(1 + c(2A_2M - f')) \quad (3)$$

where D_t = the translational diffusion coefficient at concentration c , D_0 = the diffusion coefficient extrapolated to zero concentration, A_2 = the second virial coefficient (a temperature-dependent correction term used to quantify and describe non-specific interaction potentials between particles in solution), M = molecular weight and f' = a first order frictional coefficient. In the case where $D_t > D_0$, it is usually indicative that a cluster diffuses faster in a given solvent medium, and thus gives rise to an apparently smaller radius. In this case, the correctional term $c(2A_2M - f')$ will have a large positive value. This apparent decrease in R_h at higher concentrations can be explained by the high value for A_2 . The positive increase of A_2 points to an overall increase in the repulsive forces between clusters. Essentially this exerts an additional force on the particles, causing them to move faster compared to the case of non-interacting particles. Conversely, in the situation where $D_t < D_0$, a cluster is diffusing slower than expected, and a larger R_h would be measured. In this case the opposite is true and would exhibit a large negative value for $c(2A_2M - f')$. In the situation, the cause for the apparent increase in R_h can usually be attributed to either an increase in the physical size of the species observed or an increase in the sample viscosity. To solve this problem, one can simply measure and incorporate the bulk sample viscosity in the Stokes-Einstein equation. After correcting for this viscosity, if R_h is larger than expected, then this likely leads to the scenario in which A_2 is negative and aggregation is occurring.

To elaborate further on the significance of electrostatic interactions, recall that DLS measures the translational diffusion directly, not R_h . The Stokes-Einstein relationship assumes a hard sphere undergoing Brownian motion in a dilute, non-interacting environment. This condition no longer applies when electrostatic interactions are prominent. When equally charged molecules (particularly highly charged molecules) approach one another, repulsion occurs and promotes particle acceleration. Since the Stokes-Einstein relationship assumes faster diffusion, this results in a smaller observed (or apparent) hydrodynamic radius. Experimentally, this can be tested and even mitigated by either sample dilution or by increasing the ionic strength of the solution, though the latter may potentially alter aggregation states or stability of a cluster (as the previously discussed ion-pair interactions in niobate clusters would suggest).

Effects from a significant increase in viscosity will also change the results in that a viscous solution will slow down the rate of diffusion and lead to a calculated R_h that is larger than may be expected. On the other hand, if viscosity is very fluid, this can result in a smaller observed R_h . In this scenario, it cannot be assumed that solution viscosity of a cluster is equal to that of the solvent's viscosity. Thus, it is very critical at higher concentrations to have accurate viscosity data in order to ensure accurate size results. In summary, DLS is powerful complementary techniques when utilized properly to qualitatively study clusters in solution.

3.3 Phase analysis light scattering (PALS). Massively-parallel phase analysis light scattering, commonly referred to as PALS, is another light scattering technique that is predominantly used to accurately determine the electrophoretic mobility (μ_e), zeta potential (ζ), and ionic conductivity of a species in solution. In a given PALS experiment, electrophoretic mobility measurements are acquired by illuminating a sample in a chamber with two electrodes under an alternating electrical field while collecting the scattered light. A reference beam and a redirected

second laser beam (or local oscillator) are mixed (heterodyned) directly on the detectors with scattered light from the sample and act both as an optical amplifier and as a phase reference. In such a configuration, PALS is an interferometry method in which one end of the instrument is the modulated local oscillator and the other is the scattered light.

The main disadvantage of the technique is that PALS generally suffers from many of the same drawbacks that are present with DLS, particularly if one is measuring R_h simultaneously. The biggest potential pitfall however comes with samples at high concentrations (generally above 100 mM) which can be quite conductive (conductivity ≥ 10 mS/cm). At such a high conductivity, a sample becomes increasingly susceptible to electrolysis, which would make any analysis completely unreliable. μ_e is a first-principle physical measurement that makes no assumptions regarding the shape, size, etc. for a given species. It is defined as the velocity (v) at which a charged particle moves under the influence of a spatially uniform electric field (E) (equation 4):

$$\mu = \frac{v}{E} \quad (4)$$

In the special case of spherical particles, the opposing frictional force ($F_f \propto 6\pi\eta R_h v$) to the electrical force applied ($F_e \propto QE$, where Q is the charge of the particle) is proportional to the hydrodynamic radius (R_h) of the particle, its velocity (v) and the solution viscosity (η). Under this condition, μ_e can be expanded into equation 5:

$$\mu = \frac{v}{E} = \frac{Q}{6\pi\eta R_h} \quad (5)$$

μ_e is a particularly useful value in that the zeta potential can be derived using Henry's law (equation 6):

$$\mu = \frac{2\varepsilon\zeta}{3\eta} f(\kappa R_h) \quad (6)$$

where ε = dielectric constant, ζ = zeta potential, η = viscosity, κ = Debye-Hückel parameter, and $f(\kappa R_h)$ = Henry's function.

Aqueous molecular and non-molecular clusters without a source of external stabilization (e.g., surfactants, supporting ligands) are typically stabilized as charged ions in solution. A given charged cluster will have high density of oppositely charged layers of ions surrounding it, otherwise simply referred as the electrical double layer (surface potential). The surrounding "Stern layer" is less densely charged, but contains tightly bound ions. When the molecules diffuse, both the electrical double layer and the Stern layer will move along with the molecules. This boundary that exists at the Stern layer is called the slipping or shearing plane. The electrokinetic potential of a molecule at this slipping plane is defined as the zeta potential (Figure 13).

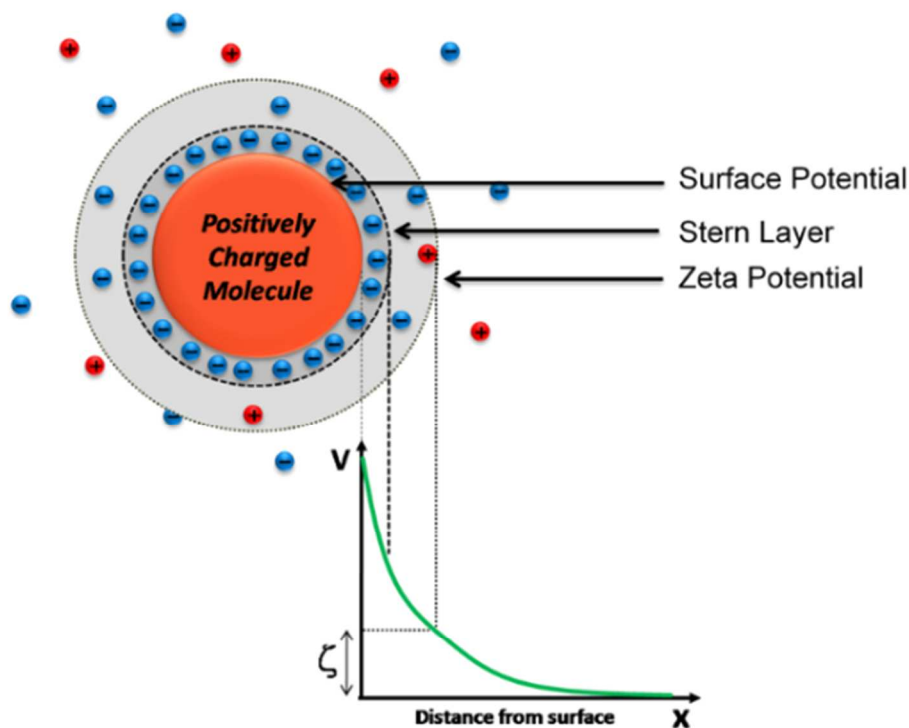


Figure 13. Simple model of a charge particle and its surrounding charges.⁹⁰ The intermediate distance away from the surface at which the surrounding ions release from the core particle's attractive pull and "slip" into equilibrium is defines where the zeta potential is found.

The primary significance of the value of zeta potential is that it is a predictor of cluster stability in solution. While aggregation of clusters can readily be monitored by DLS and SAXS over time, such long term stability or accelerated aging studies are simply time consuming. Regardless, the magnitude of the zeta potential indicates the degree of electrostatic repulsion between similarly charged clusters in solution. In other words, the higher the zeta potential, the more stable a cluster will be. Generally, a cluster can be predicted to have prolonged stability if the magnitude of the zeta potential is greater/less than ± 30 mV. At such high potential values, the repulsive forces will exceed the attractive forces and ultimately allow a cluster to exist as its own discrete species. However, as the magnitude of zeta potential approaches zero, the force of attraction becomes greater than the overall repulsive forces and leads toward rapid instability and flocculation. Zeta potential is particularly useful for cluster analysis in that it provides a direct measure of the isoelectric point (pH at which the charge is 0 mV) and can be corroborated with conductivity and size measurement to further understand phenomena such ion association.

To complement the **HafSO_x** cluster study mentioned in the previous SAXS and DLS sections, initial zeta potential measurement taken of both **HafSO_x** with and without added H₂O₂ revealed that the **HafSO_x** mixture without H₂O₂ had a zeta potential of $10.3 \text{ mV} \pm 1.56 \text{ mV}$ while the addition of H₂O₂ to **HafSO_x** increased this value to $28.6 \text{ mV} \pm 2.3 \text{ mV}$. This indicates that H₂O₂ plays a major role in charge stabilization for this particular cluster species. Predictably, the **HafSO_x** solutions that contain no H₂O₂ began to polymerize within a day and crystallized out of solution soon after.

Studies have also been done to determine the isoelectric point of $\mathbf{f-AlI_3}$ using PALS. In this study, 50 mM $\mathbf{f-AlI_3}$ was titrated with 100 mM NH_4OH from a pH range of 3.5 up to 9, where the zeta potential for $\mathbf{f-AlI_3}$ was found to be 0 mV and is by definition the isoelectric point (Figure 14).

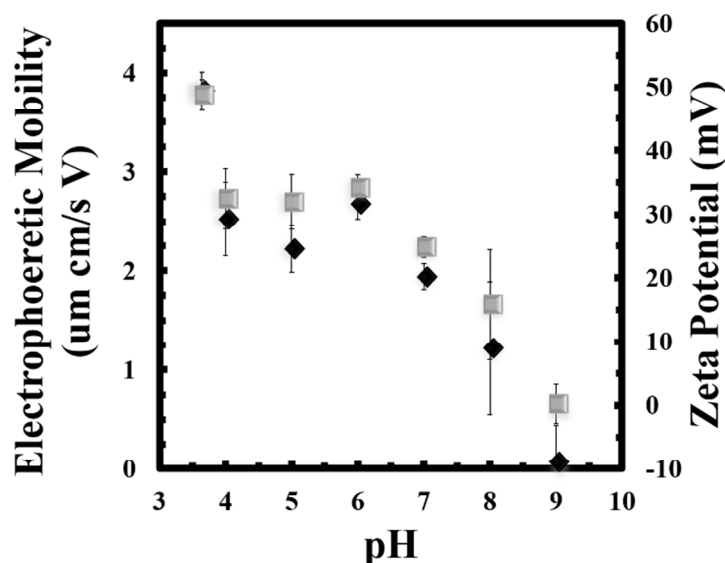


Figure 14. Plot of electrophoretic mobility (black diamonds) and zeta potential (grey squares) vs pH of $\mathbf{f-AlI_3}$. Mobility data is shown to demonstrate the direct relationship it has with zeta potential. The isoelectric point for $\mathbf{f-AlI_3}$ is shown to be at pH = 9.

Interestingly, although agglomeration of the cluster is quite prevalent with the addition of NH_4OH (simultaneous DLS measurement revealed a size increase from 1 nm to ~ 5 nm), the solutions were shown to still have a fairly high charge of around 35 mV between the pH ranges of 4 to 6. Subsequent flocculation does not occur until around a pH of 8 as the cluster reaches its isoelectric point at a pH of ~ 9 . To conclude, PALS is an excellent tool for predicting cluster stability in solution and can be utilized with virtually any other solution technique to explore and understand the complex nature of charge speciation and dependency in solution.

3.4 Raman Spectroscopy. Since its discovery by Dr. C. V. Raman in 1928, Raman spectroscopy has been recognized as a very important analytical tool across numerous

disciplines. Due to its sensitivity, high information content, and non-destructive nature, applications span many fields of chemistry and materials science.^{91,92} Often paired with IR, both techniques are used complementarily to probe different aspects of a given sample. For instance, while IR is typically sensitive to functional groups and to highly polar bonds, Raman is more sensitive to backbone structures and symmetric bonds. Using both techniques provides twice the information about the vibrational structure than can be obtained by using either technique alone. In addition to providing unique information about a sample, Raman offers several additional benefits, including: minimal to no sample preparation, sampling directly through glass, non-destructive analysis (with exception of light-sensitive materials), non-intrusive analysis, permitting study of more labile sample features (such as crystal structure), and minimal interference from IR-active species such as H₂O or CO₂.

In Raman spectroscopy, the sample is irradiated with monochromatic light and the photons emitted are either elastically (Rayleigh) or inelastically (Raman) scattered. The inelastically scattered light has lost (Stokes) or gained (anti-Stokes) energy during this interaction and the emitted photon contains information about the molecular structure of the sample, particularly the vibrational modes of a molecule. Since Raman scattering is extremely weak in relation to Rayleigh scattering (1:~10⁷ photons will be Raman scattered), filters are used to limit the observed intensity of the Rayleigh scattering. The other requirement for a vibration to be Raman active is that a given molecular vibration must give rise to a distortion of the electron cloud that surrounds the molecules under the influence of an electric field (polarizability).

While Raman spectroscopy has been widely used in characterization of organic, organometallic and biological molecules among many others, it has been used less frequently in the search to identify inorganic cluster species. For our particular interest, we seek to use this

technique as a means for rapid identification of clusters, establishing a database of known clusters in the solid state, screening for potential new targets, and qualitatively and quantitatively investigating the speciation and dynamics of clusters in solution. One can immediately observe qualitative differences between the various vibrational modes in the Raman spectra of crystalline bismuth nitrate and the $\text{Bi}_6\text{O}_4(\text{OH})_4(\text{NO}_3)_6 \cdot \text{H}_2\text{O}$ cluster (Figure 15).⁹³

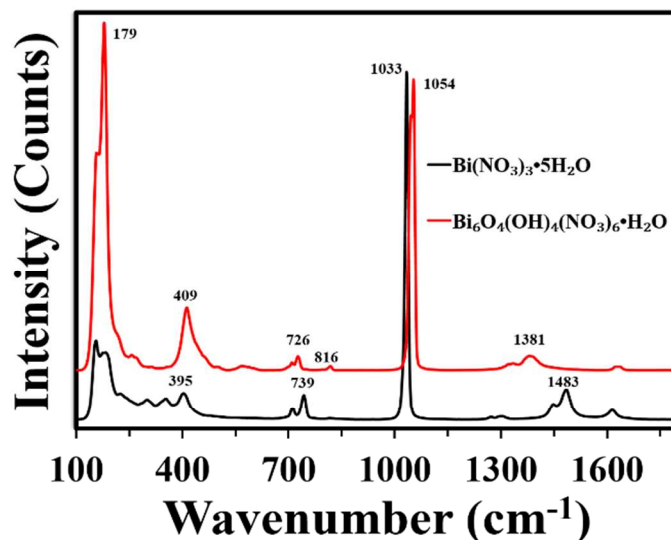


Figure 15. Stacked Raman spectra of Bismuth nitrate (black) and a bismuth hexamer (red).⁹³ Notable peaks that distinguishes this cluster from bismuth nitrate include the two stretching Bi—O bands at 179 cm^{-1} and 409 cm^{-1} . The small peak at 816 cm^{-1} corresponds to a $\mu\text{—OH}$ bridge of the cluster. Additionally, spectral shifts of the symmetric and anti-symmetric bands of NO_3^- ion are present. The symmetric stretching band at 1033 cm^{-1} for $\text{Bi}(\text{NO}_3)_3$ is blue shifted to 1054 cm^{-1} while the anti-symmetric band at 1483 cm^{-1} for $\text{Bi}(\text{NO}_3)_3$ is red shifted to 1381 cm^{-1} for the bismuth cluster.

Since crystal structures of both species have been determined, solid state Raman data can be generated for each cluster, which then provides a means of identifying the species in solution and gaining insight on the cluster speciation through solution Raman spectroscopy. However, this can become increasingly complicated when an exact structure is unknown or when there is little precedent available for an unknown sample. To circumvent such problems, complementary methods such as quantum mechanical computations (discussed below) serve as a powerful tool towards understanding spectral data.

Raman spectroscopy also allows for qualitative and quantitative investigations of many facets of the dynamic nature of clusters in both the solid state and solution. More specifically, it is useful for studying changing speciation as a result of metal exchange, chemical equilibria, temperature changes, pH changes, solvent effects, as well as observing the formation of clusters from their precursor monomers.⁹⁴ For instance, the dissociation mechanism of the **f-Al₁₃** cluster in aqueous solution can be studied by Raman spectroscopy. In this particular study (Figure 16) the dissociation/decomposition of **f-Al₁₃** to Al(NO₃)₃ is observed by Raman during the titration of **f-Al₁₃** with HNO₃, as indicated by the appearance of the Al–O symmetric stretch at 525 cm⁻¹ known for Al(OH₂)₆³⁺.^{95,96}

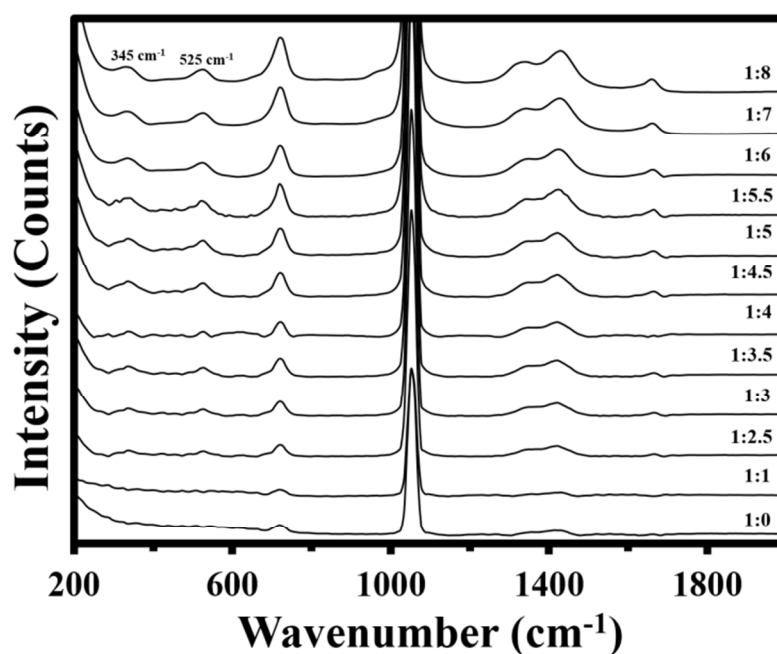


Figure 16. Stacked Raman spectra of **f-Al₁₃** titrated with various equivalents of HNO₃. The bottom spectrum represents a solution of 1 M **f-Al₁₃** with no added HNO₃ as indicated by the ratios shown on the right of the graph.

A second peak at 345 cm⁻¹ can also be described as an antisymmetric Al–O vibration. Importantly, while it is possible to quantify data like that shown in Figure 19, one must be aware of some of the challenges that are prevalent with solution quantification using Raman. An

immediate problem that arises is the fact the many of the molecular vibrations, particularly in solution, associated directly with a cluster of interest (i.e., M–O, M–OH, M–H₂O, etc.) are often several orders of magnitude weaker than overlapping peaks of the counterions or solvent. To combat this issue, techniques such as accumulation of longer scan times and advanced background subtractions such as removing the influence of the solvent peaks are often employed to reveal some of the weaker Raman scatters (as shown in Figure 19).⁹⁶ A recent study also utilized differential background subtractions to monitor *in situ* the growth of **f-Al₁₃** from Al(NO₃)₃ via electrochemical titration.⁹⁴ With such a technique, it was revealed that an initial “Al₇” core is established prior to the formation of **f-Al₁₃** and that the Al₇ core exists in solution with the **f-Al₁₃** cluster. In summary, Raman spectroscopy is a relatively facile, but powerful technique to use in conjunction with other methods to explore complex fundamental questions associated with many aqueous inorganic clusters.

4 COMPUTATIONAL STUDIES

With the increase in computing power and improvements in theoretical methods over the last several decades, quantum mechanical computations have demonstrated their potential to inform and predict. When used properly, computations can prove to be powerful, assisting in the understanding of the structural properties, thermodynamic stabilities, vibrational spectra, dynamics, and electronic properties of nanoscale clusters and particles.

4.1. Vibrational Spectroscopy. Vibrational spectroscopy is a common technique for characterizing nanoscale clusters and appealing for analyzing nanoscale materials due to the relative ease with which these spectra can be collected.⁹⁵ For most nanoscale clusters, the assignment of signals, and ultimately the elucidation of exactly what species are present in

solution is difficult, if not impossible, without computations. Computations can be used to identify signature peaks for specific functional groups, allowing for identification of species with unique functional groups in subsequent experiments.

In practice, IR and Raman are straightforward to compute.⁹⁷ Computing these modes is a relatively simple process when a few factors are kept under consideration. First, the structure of a species needs to be properly optimized to the ground state before computing its vibrational modes. Poorly optimized structures or structures taken directly from crystals will yield nonsensical vibrational frequency values. Often, crystal structures cannot be used directly because the effect of the crystal lattice on the geometry is significant enough that one cannot always assume that the ground state geometry of the species remains constant from crystal to solution or gas phase.

Once the vibrational modes have been correctly computed, there are several steps required to produce a computed spectrum that is directly comparable to the experimental. Most crucially, peak broadening must be accounted for, as these effects are not treated at all in normal mode analyses of commercially available computational software packages. We have resorted to numerical fitting methods to introduce peak broadening to produce computed vibrational spectra that are more easily compared to experiments with great success. Procedurally, each vibrational peak is fit to a Gaussian function. The computed frequency and intensity of each vibration are constant and scaled with concertedness. The widths of the vibrations are allowed to independently vary, within an accepted range of values, until the deviation between the computed and experimental spectra are minimized. It is important to limit the variation of width values; otherwise, the numerical solution found may be non-physical in nature. Vibrational widths may either become very narrow or wide if they are not limited, resulting in peaks that become too

narrow and essentially disappear or become wide enough that they no longer represent a reasonable physical solution

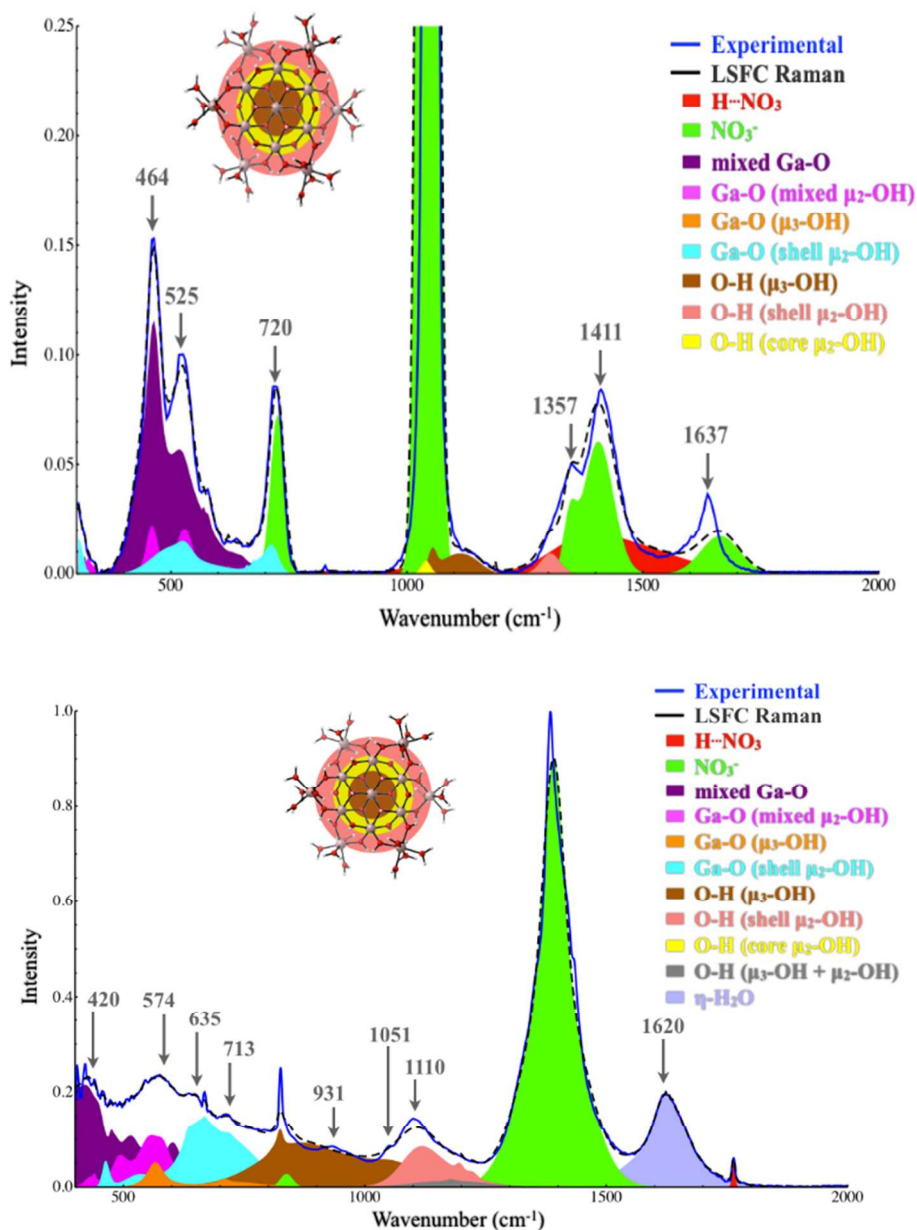


Figure 17. Top. Simulated and experimental IR overlay spectra from 500 cm^{-1} – 2000 cm^{-1} of solid state **f-Ga₁₃**. Bottom. Simulated and experimental Raman spectra from 200 - 2000 cm^{-1} of crystalline **f-Ga₁₃** at $25\text{ }^{\circ}\text{C}$. The feature shown at 464 cm^{-1} arises from the primary breathing mode of the cluster.

This method has been used on a wide array of systems, from organic molecules to metal oxide and hydroxide clusters. This technique was applied to interpreting the IR and Raman

signals of aqueous and solid samples of gallium and aluminum tridecameric hydroxide clusters, $[M_{13}(OH)_{24}(H_2O)_{24}](NO_3)_{15}$ or **f-M₁₃** (Figure 17). This analysis procedure led to the full assignment of each spectrum and led to identification of each cluster's unique signals in both solid and aqueous samples. Unsurprisingly, this analysis worked better for solid samples than for aqueous solutions. The structure of these clusters is much better characterized in the solid state than in solution, including the understanding of protonation state and position of counterions. In solution, unlike the solid state, there also may be small amounts of other species present, as the cluster has the ability to fragment into smaller clusters and monomers in solution. This spectral fitting method has also been demonstrated for the α - and β -Keggin phosphomolybdate anions, where the authors studied the IR of the Keggin phosphomolybdate anion with the goal of determining the identity of the isomer of the anion by computing the IR of both the α - and β -isomers. The computed spectra for both of these anionic clusters were in reasonable agreement with the experimental IR spectrum, with each of the significant experimental peaks described by an analogous computed vibrational mode. However, the computed spectra of the α - and β -isomers were too similar to allow for unique identification of isomers via IR.⁹⁷ This conclusion highlights the limitations of using computations and vibrational spectroscopy to uniquely identify clusters.

4.2 Thermodynamic Stability. The thermodynamic stability of clusters is conceptually one of the easiest calculations to perform and interpret. The Gibbs free energy of each species is directly computed and provided as a scalar value in the results of most normal mode analyses. However, the challenge of thermodynamic stability is in knowing which method will yield accurate results with respect to experiments. In addition, it is often difficult to properly determine the appropriate environment including counterions and implicit or explicit solvent, which significantly

complicates matters. Often, the number of possibilities for the positions of counterions and solvent, as well as concerns for protonation states, makes the determination of the lowest energy structure extremely time-consuming.

There have been many studies examining the stability of nanoscale polyoxometalate clusters. The Keggin cluster family is a popular topic of study because this family of clusters has five different isomers based on the rotation of a trimeric group at the exterior of the cluster. Understanding the stability of these clusters is important for understanding the likelihood of synthesizing one isomer over another, especially if only one isomer is well-suited for a particular application. For the Keggin phosphotungstates, computations were able to reveal the stability of each of the five isomers.⁹⁹ When examining this stability trend, the authors found that the stability of each isomer was largely determined by how many unfavorable W-W contacts each isomer had, as each contact contributed approximately 8-9 kcal/mol in destabilization. A similar trend was computed for phosphomolybdate Keggin ions, though with a slightly lower destabilization energy per metal-metal contact.¹⁰⁰

The geometries of ionic nanoscale species are strongly affected by solvation effects. This effect is particularly pronounced in aqueous solutions and particularly for species that are strong hydrogen bond donors or acceptors. In the case of metal hydroxo clusters, these clusters tend to optimize to geometries where intramolecular hydrogen bonding between water and hydroxo ligands are more significant than are expected in the aqueous solution, even with the use of implicit solvent models such as PCM and COSMO.^{101,102} The formation of these intramolecular hydrogen bonds tends to lead to structures that exhibit significantly distorted bond angles. Explicit counterions and solvents can help to reduce these structural distortions; however, counterions alone may not be sufficient to fix these distortions. Minute changes can lead to large

differences in the optimized structures, so it is important to understand all of the factors that could affect structure, including exact sites of protonations and locations of counterions & solvents.

4.3 Dynamics. Molecular dynamics computations have the potential to solve a wide variety of problems. These can be divided into two general categories relating to the method of generating the Hamiltonian: molecular mechanics (MM) molecular dynamics (MMMD) or ab-initio molecular dynamics (AIMD).. The MMMD approach is much less computationally demanding because the forces are computed using simple Newtonian forcefield models (ball and spring). Thus MMMD can be and has been applied to study extremely large systems (e.g. the giant polyoxometalate Mo_{132}),¹⁰³ where quantum mechanical computations would be unable to yield results in a reasonable time frame. Historically, these simulations have been useful in examining the diffusion of different species in solution and the interaction of these species with solvent molecules.⁹⁷ In addition, it has also been used to understand average coordination environments of metal ions, which can provide information about the mechanism of cluster formation.¹⁰²

AIMD has the potential to inform scientists about a variety of solution behaviours not captured by MMMD (e.g. bond breaking, proton transfer, etc.). However AIMD has yet to be used on a routine basis on nanoscale systems. One of the more appealing options is the use of mixed or hybrid quantum mechanical and molecular mechanical computations (QM/MM).¹⁰³ These types of computations are particularly appealing because they have the potential to provide the best of both worlds – accurate chemistry of the AIMD and the superior efficiency of the MMMD. This is appealing for looking at systems where the explicit solute-solvent interactions are of material interest to the chemistry.¹⁰⁴

4.4 Electronic Properties. Electronic properties of materials are typically probed using density functional theory (DFT). Obtaining orbital energies, sizes, and shapes are trivial from static DFT. Optical gaps are often probed using the time-dependent variant (TD-DFT). Optical gaps can be obtained from many methods and basis sets with high accuracy; however, the accurate determination of fundamental gaps requires more specialized methods.¹⁰⁸

The most practical applications of computing the electronic properties of nanomaterials are to determine the redox chemistry. This has been done extensively on a wide range of nanomaterials, from polyoxometalate clusters to nanoparticles.¹⁰⁶⁻¹⁰⁹ Polyoxometalates and nanoparticles often make good oxidizing agents.^{97,110} DFT can also be used to compute the HOMO-LUMO gaps of clusters.^[104] and these can be used to estimate the relative ability of multiple species to act as oxidizing agents. The exact values for the HOMO-LUMO gaps cannot be used to determine the experimental redox potential without further information. Much like in experiments, the redox potential must always be described as relative to another reaction, in most cases, the standard hydrogen electrode. To reproduce these values computationally, the reaction of interest needs to be compared to the computed analog of the standard hydrogen electrode.¹¹¹ When properly computed, these calculations can be used to determine the relative oxidizing ability of many different agents and determine the one most suited for a particular application without ever having to enter a laboratory.

4.5 NMR. The NMR signals of nanoscale species can be and has been studied by computations, but these studies are limited by many of the same factors as the previous studies, particularly for solution NMR studies. These are incredibly sensitive to solvent, especially if the solvent being used for NMR is different than the solvent used for synthesis. The identity and specific interactions with counterions also significantly complicate matters. In addition, in

structures optimized with full QM, equivalent atoms by cursory inspection of symmetry involving non-hydrogen atoms may not retain the symmetry after the geometry optimization is completed. Formation of intramolecular hydrogen bonds and positions of counterions also significantly complicate matters. Depending on the proton exchange kinetics and conformational flexibilities, these high-symmetry structures may not be representative of the average structure seen on the NMR time-scale and hence yield inconsistent chemical shifts to experiments.

Despite these challenges, several studies have been reported, aimed at predicting the relative NMR shifts of various nuclei. The full proton assignment for the aqueous gallium and indium mixed metal tridecamers has been realized using computations, as discussed previously. However, in this work and the study of ^{183}W NMR shifts of several POMs,¹¹⁶ the correct ordering of chemical shifts were obtained, but the quantitative values of the chemical shifts could not be reproduced. In addition to these studies, computations have been used to compare theoretical shifts for similar size aqueous aluminium clusters.¹¹⁵ However, experimental corroboration for these computed shifts has not been obtained. Computations have also assisted in understanding the solid state NMR of Group 13 tridecamers, also discussed previously. These studies have been useful in understanding the NMR of many inorganic nanoscale species; however, there is a large amount of work that remains to accurately reproduce quantitative chemical shifts of these species.

CONCLUSIONS

The grand challenges that exist aimed at understanding the basic fundamental chemistries of the many clusters that preside in nature or through controlled synthesis offer a unique opportunity for researchers to explore and to develop new methods for analysis. In this Perspective we have surveyed some of the emerging combinations of venerable and new

techniques that are finding utility currently. Rapid development of new and improved analytical technology and improved basic science understanding are still required for us to delve even deeper as we continue to characterize and explore the dynamics of aqueous inorganic clusters in the solid state and solution, and to provide improved resolution on the speciation of metal ions and their clusters in polar solvents. As one example, **f-Al₁₃** does not appear on speciation diagrams of aqueous Al hydrolysis; however, the abundance of emerging evidence studying this cluster over wide concentration and pH ranges suggests that this cluster (and perhaps many others) remain to be discovered during controlled metal ion hydrolysis.

ACKNOWLEDGMENTS

This material is based on work in the Center for Sustainable Materials Chemistry, which is supported by the U.S. National Science Foundation under Grant CHE-1102637. We gratefully acknowledge the use of UO CAMCOR facilities, which have been purchased with a combination of federal and state funding. D.W.J. is a Scialog Fellow of Research Corporation for Science Advancement. We would like to thank Wyatt Technology for providing helpful discussions in explaining the schematic concepts for dynamic and phase analysis light scattering in this review, and specifically in Figure 16 in the phase analysis light scattering section. We acknowledge Dolly W. Zhen for conducting isoelectric point studies on **f-Al₁₃** using phase analysis light scattering as well. Lastly, we thank Alexia G. Smith for performing experiments on **f-Al₁₃** to Al(OH₂)₆³⁺ dissociation studies using Raman spectroscopy and dynamic light scattering analysis on Al(NO₃)₃ in aqueous solution. Research on the [(UO₂)₂₄(O₂)₂₄(P₂O₇)₁₂]⁴⁸⁻ molecule was supported by the Office of Basic Energy Science of the U.S. Department of Energy as part of the

Materials Science of Actinides Energy Frontier Research Center (DE-SC0001089) (subcontract to WHC).

NOTES AND REFERENCES

^a Department of Chemistry & Biochemistry and the Materials Science Institute, University of Oregon, Eugene, Oregon 97403-1253, USA.

Fax: 541-346-0487; Tel: 541-346-1695; E-mail: dwj@uoregon.edu

^b Department of Chemistry, Washington University, St. Louis, Missouri 63130-4899, USA.

E-mail: hayes@wustl.edu

^c Department of Chemistry, Oregon State University, 153 Gilbert Hall, Corvallis, OR 97331-4003, USA. E-mail: paul.cheong@oregonstate.edu; May.Nyman@oregonstate.edu

^d Departments of Chemistry and Geology, University of California, Davis, One Shields Ave., California 95616 Email: whcasey@ucdavis.edu

† The Bloch-McConnell equations are a coupled system of differential equations that account for changes in magnetization ($M_w'(t)$ and $M_m'(t)$) as a function of time as the sites exchange magnetism:

$$\frac{d}{dt} \begin{pmatrix} M_w'(t) \\ M_m'(t) \end{pmatrix} = -(i\bar{L} + \bar{R} + \bar{K}) \begin{pmatrix} M_w'(t) \\ M_m'(t) \end{pmatrix} \quad (1)$$

where:

$$\begin{aligned} \bar{L} &= \begin{pmatrix} \Delta\omega_w & 0 \\ 0 & \Delta\omega_m \end{pmatrix} \\ \bar{R} &= \begin{pmatrix} \frac{1}{T_{2,w}} & 0 \\ 0 & \frac{1}{T_{2,m}} \end{pmatrix} \\ \bar{K} &= \begin{pmatrix} k_w & -k_m \\ -k_w & k_m \end{pmatrix} \end{aligned} \quad (2)$$

and the parameters are: are the difference in resonance frequencies of the two sites, here abbreviated 'w' for water and 'm' for metal, are the corresponding rates of transverse relaxation and k_i are the (usually first-order) rate coefficients for chemical exchange. The resulting system of coupled linear differential equations takes on the general solution:

$$\begin{pmatrix} M'_w(t) \\ M'_m(t) \end{pmatrix} = \exp[-(i\bar{L} + \bar{R} + \bar{K}) t] \begin{pmatrix} M'_{w,0} \\ M'_{m,0} \end{pmatrix} \quad (3)$$

Where parameters $M'_{w,0}$ and $M'_{m,0}$ correspond to the initial magnetization of water and the bound waters immediately *after* the pulse. This solution describes the transverse magnetization in the time domain, which oscillates and decays with time. These equations are solved numerically to yield fits to intensity data, such as those shown in Figure 3B, yielding rate coefficients.

1. (a) S. L. Cumberland, K. M. Hanif, A. Javier, G. A. Khitrov, G. F. Strouse, S. M. Woessner, C. S. Yun, *Chem Mater*, 2002, **14**, 1576; (b) H. Ogino, S. Inomata, H. Tobita, *Chem Rev*, 1998, **98**, 2093; (c) S. Dehnen, M. Melullis, *Coordin Chem Rev*, 2007, **251**, 1259.
2. (a) G. E. Kostakis, A. M. Ako, A. K. Powell, *Chem Soc Rev*, 2010, **39**, 2238; (b) G. E. Kostakis, S. P. Perlepes, V. A. Blatov, D. M. Proserpio, A. K. Powell, *Coordin Chem Rev*, 2012, **256**, 1246.
3. (a) R. Sessoli, A. K. Powell, *Coordin Chem Rev*, 2009, **253**, 2328; (b) M. Viciano-Chumillas, S. Tanase, J.L. de Jongh, J. Reedijk, *Eur. J. Inorg. Chem.*, 2010, 3403.

4. (a) M. T. Pope, A. Muller, *Angew. Chem. Int. Edit.*, 1991, **30**, 34; (b) Baker, L. C. W.; Glick, D. C. *Chem. Rev.*, **1998**, *98*, 3; (c) A. Muller, P. Kogerler, A. W. M. Dress, *Coordin. Chem. Rev.*, 2001, **222**, 193; (d) M. Nyman, *Dalton T.*, 2011, **40**, 8049.
5. Z. L. Mensinger, W. Wang, D. A. Keszler, D. W. Johnson, *Chem. Soc. Rev.*, 2012, **41**, 1019.
6. (a) F. C. Meldrum, H. Cölfen, *Chem. Rev.* 2008, **108**, 4332; (b) A. Navrotsky, *Proc. Natl. Acad. Sci. U. S. A.* 2004, **101**, 12096; (c) L. Addadi, S. Raz, S. Weiner, *Adv. Mater.* 2003, **15**, 959; (d) A. Legg, M. Q. Zhu, L. R. Comolli, B. Gilbert, J. F. Banfield, *Langmuir* **2014**, **30**, 9931; (e) M. Q. Zhu, B. Legg, H. Z. Zhang, B. Gilbert, Y. Ren, J. F. Banfield, , G. A. Waychunas, *Environ. Sci. Technol.*, 2012, **46**, 8140.
7. D. Grandjean, A. M. Beale, A. V. Petukhov, B. M. Weckhuysen, *J. Am. Chem. Soc.*, 2005, **127**, 14454.
8. (b) A. Kalaji, S. Skanthakumar, M. G. Kanatzidis, J. F. Mitchell, L. Soderholm, *Inorg. Chem.* 2014, **53**, 6321; (c) L. A. Chivacchi, C. Bourgaux, V. Briois, S. H.; Pulcinelli, C. V. Santilli, *J. Appl. Crystallogr.* 2000, **33**, 592; (d) L. A. Chivacchi, S. H. Pulcinelli, C. V. Santilli, V. Briois, *Chem. Mat.* 1998, **10**, 986; (e) L. A. Chivacchi, C. V. Santilli, S. H. Pulcinelli, C. Bourgaux, V. Briois, *Chem. Mat.* 2004, **16**, 3995; (f) L. A. Chivacchi, C. V. Santilli, S. H. Pulcinelli, A. F. Craievich, *J. Appl. Crystallogr.* 1997, **30**, 750.
9. A. F. Oliveri, M. E. Carnes, M. M. Baseman, E. K. Richman, J. E. Hutchison, and D. W. Johnson, *Angew. Chemie Int. Ed.*, 2012, **51**, 10992.

10. A. F. Oliveri, E. W. Elliott, M. E. Carnes, J. E.; Hutchison, Johnson, D. W., *ChemPhysChem.*, 2013, **14**, 2655.
11. Z. L. Mensinger, J. T. Gatlin, S. T. Meyers, L. N. Zakharov, D. A. Keszler, D. W. Johnson, *Angew. Chem. Int. Ed.*, 2008, **47**, 9484.
12. M. Alemayehu, J. E. Davis, M. Jackson, B. Lessig, L. Smith, J. D. Sumega, C. Knutson, M. Beekman, D. C. Johnson, D. A. Keszler, *Solid State Sci.* 2011, **13**, 2037.
13. B. Bogdan Botar, A. Ellernb, P. Kögerler, *Dalton Trans.*, 2012, **41**, 8951.
14. L. Moreno-Real, E.R. Losilla, M.A. Aranda, M. Martinez-Lara, S. Bruque, M. Gabas, *J. Solid State Chem.* 1998, **137**, 289-294.
15. N. E. Jacobsen, *NMR Spectroscopy Explained: Simplified Theory, Applications and Examples for Organic Chemistry and Structural Biology*, John Wiley & Sons, Inc., 2007.
16. L. Ronconi and P. J. Sadler, *Coord. Chem. Rev.*, 2008, **252**, 2239.
17. R. V. Parish, *NMR, NQR, EPR, and mossbauer spectroscopy in inorganic chemistry*, Ellis Horwood Limited, Chichester, West Sussex, 1990.
18. Z. L. Ma, K. M. Wentz, B. A. Hammann, I.-Y. Chang, M. K. Kamunde-Devonish, P. H.-Y. Cheong, D. W. Johnson, V. V. Terskikh, and S. E. Hayes, *Chem. Mater.*, 2014, **26**, 4978.
19. L. Allouche, C. Huguenard, and F. Taulelle, *J. Phys. Chem. Solids*, 2001, **62**, 1525.
20. L. Allouche, C. Gerardin, T. Loiseau, G. Ferey, and F. Taulelle, *Angew. Chemie Int. Ed.*, 2000, **39**, 511.

21. L. Allouche and F. Taulelle, *Inorg. Chem. Commun.*, 2003, **6**, 1167.
22. W. H. Casey, *Chem. Rev.*, 2006, **106**, 1.
23. G. Fu, L. F. Nazar, and A. D. Bain, *Chem. Mater.*, 1991, **3**, 602.
24. G. Furrer, B. L. Phillips, K.U. Ulrich, and R. Pöthig, *Science*, 2002, **297**, 2245.
25. L. J. Michot, E. Montargès-Pelletier, B. S. Lartiges, J.B. d'Espinose de la Caillerie, V. Briois, *J. Am. Chem. Soc.*, 2000, **122**, 6048.
26. W. O. N. Parker, R. Millini, and I. Kiricsi, *Inorg. Chem.*, 1997, **36**, 571.
27. B. L. Phillips, W. H. Casey, and M. Karlsson, *Nature*, 2000, 379.
28. J. W. Akitt, in *Multinuclear NMR*, ed. J. Mason, Springer US, 1987, 259.
29. J. W. Akitt, *Nuclear Magnetic Resonance Spectroscopy in Liquids containing Compounds of Aluminium and Gallium*, Elsevier, 1972, **vol. 5**.
30. F. W. Wehrli, in *Annual Reports on NMR Spectroscopy*, ed. G. A. Webb, Academic Press, 1979, **vol. 9**, 125.
31. www.webelements.com
32. A. F. Oliveri, L. A. Wills, C. R. Hazlett, M. E. Carnes, P. H-Y. Cheong, D. W. Johnson, *Chem. Sci.* **2015**, *6*, 4071-4085
33. L. Helm and A. E. Merbach, *Chem. Rev.*, 2005, **105**, 1923.
34. Y. Cohen, L. Avram, and L. Frish, *Angew. Chemie Int. Ed.*, 2005, **44**, 520.

35. R. C. Hardy and R. L. Cottington, *J. Res. Natl. Bur. Stand.*, 1949, **42**, 573–578.
36. W. N. Baker, *J. Chem. Phys.*, 1936, **4**.
37. T. D. W. Claridge, *High-resolution NMR techniques in organic chemistry*, 1999.
38. For detailed reviews on the use and optimization of DOSY NMR, the reader is referred to:
(a) M. Nilsson, G.A. Morris, *Mag. Res. Chem.* 2006; **44**, 655; (b) G. A. Morris, Diffusion-ordered spectroscopy (DOSY). In: D.M. Grant, R.K. Harris, ed. *Encyclopedia of Nuclear Magnetic Resonance*. Wiley. 2002: 35; (c) M. Nilsson, M. A. Connell, A. L. Davis, G. A. Morris, *Anal. Chem.*, 2006, **78**, 3040.
39. J. Ling, et al., *J. Am. Chem. Soc.*, 2010, **132**, 13395.
40. R.L. Johnson, et al., *Angew. Chemie Int. Ed.*, 2013, **52**, 7464.
41. J.R. Rustad, and W.H. Casey, *Nat. Mater*, 2012, **11**, 223.
42. J.R. Rustad, J.S. Loring, and W.H. Casey, *Geochim. Cosmochim. Ac.*, 2004, **68**, 3011.
43. C.A. Ohlin, *Chemistry-An Asian Journal*, 2012. **7**, 262.
44. (a) C.A. Ohlin, et al., *Dalton Trans.*, 2009, **27**, 5278; (b) M. A. Abonnenc, L. Qiao, B. Liu, H. H. Girault, *Annu. Rev. Anal. Chem.* 2010, **3**, 231; (c) M. A. Henderson, J. S. McIndoe *Int. J. Mass. Spectrom.* 2013, **354-355**, 257; (d) P. J. Dyson, B. F. G. Johnson, J. S. McIndoe, P. R. R. Langridge-Smith, *Rap. Comm. Mass. Spectrom.* 2000, **14**, 311.
45. Villa, E.M., et al., *J. Am. Chem. Soc.*, 2010, **132**, 5264.
46. C.J. Besecker, et al. *Inorg. Chem.*, 1985. **24**, 1027.

47. M. Filowitz, et al. *Inorg. Chem.*, 1979, **18**, 93.
48. M. Filowitz, et al. *J. Am. Chem. Soc.*, 1976. **98**, 2345.
49. W.G. Klemperer, *NATO ASI Series, Series C: Mathematical and Physical Sciences*, 1983, **103**, 245.
50. W.H. Casey, et al., *Geochim. Cosmochim. Ac.*, 2000, **64**, 2951.
51. E.M. Villa, et al. *Angew. Chem. Int. Ed.*, 2008. **47**, 4844.
52. E.M. Villa, et al., *J. Am. Chem. Soc.*, 2009. **131**, 16488.
53. J.R. Black, M. Nyman, and W.H. Casey, *J. Am. Chem. Soc.* 2006. 128, **45**, 14712.
54. Ohlin, C.A., et al. *Chem. Eur. J.*, 2011, **17**, 4408.
55. J.R. Houston, and W.H. Casey, *Dalton Trans.* 2005, **22**, 3667.
56. Houston, J.R., B.L. Phillips, and W.H. Casey, *Geochimica et Cosmochimica Acta*, 2006. **70**, 1636-1643.
57. W.H. Casey and B.L. Phillips, *Geochim. Cosmochim. Ac.*, 2001, **65**, 705.
58. S.J. Harley, C.A. Ohlin, and W.H. Casey, *Geochim. Cosmochim. Ac.*, 2011, **75**, 3711.
59. B. Bureau, G. Silly, J.Y. Buzaré, C. Legein, D. Massiot, *Solid State Nucl. Magn. Reson.* 1999, **14**, 181.
60. (a) K. J. D. MacKenzie; M. E. Smith. *In Multinuclear Solid-State NMR of Inorganic Materials*; R.W. Cahn. Ed.; (b) *Pergamon Materials Series*, Elsevier Science Ltd, 2002, 653.

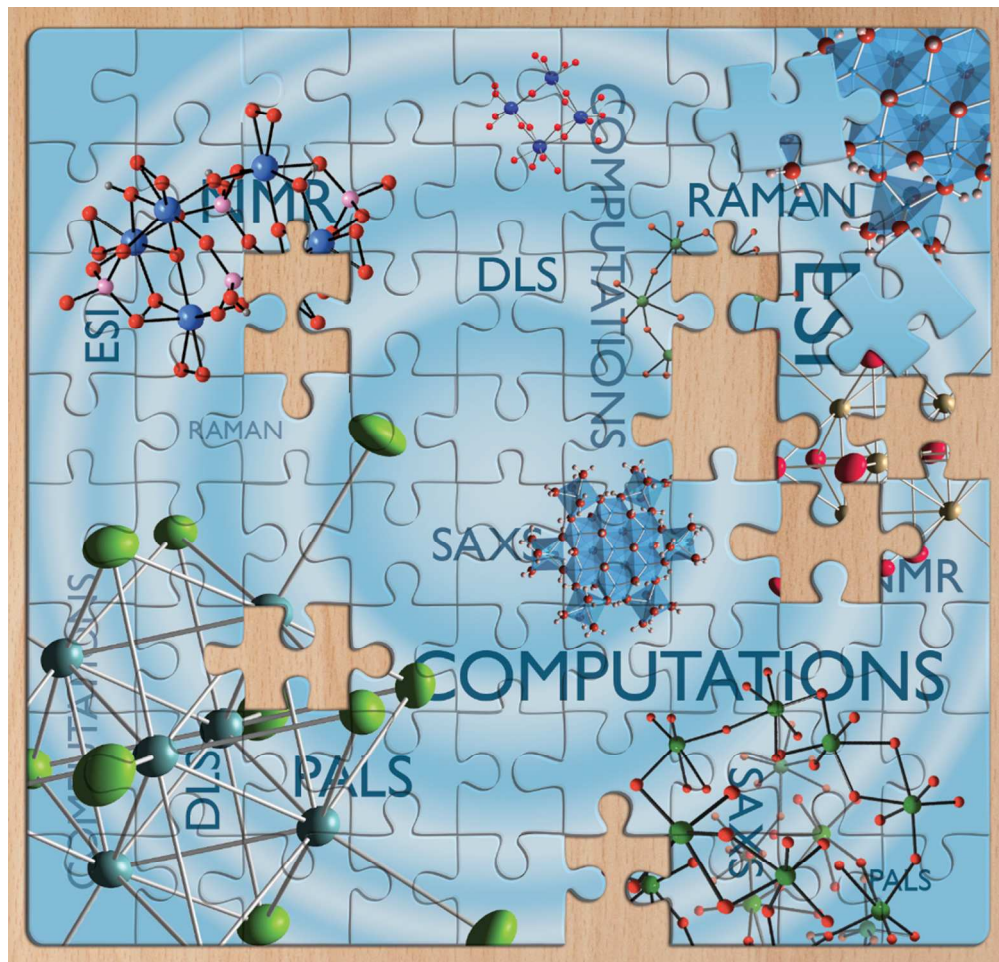
61. D. Massiot; I. Farnan; N. Gautier; D. Trumeau; A. Trokiner; J.P. Coutures. *Solid State Nucl. Magn. Reson.* 1995, **4**, 241.
62. T. Vosegaard; D. Massiot; N. Gautier; H. Jakobsen. *J. Am. Chem. Soc.*, 1998, **120**, 8184.
63. E. Rather, J.T. Gatlin, P.G. Nixon, T. Tsukamoto, V. Kravtsov, D.W. Johnson, *J. Am. Chem. Soc.* 2005, **127**, 3242.
64. D. Massiot, F. Fayon, M. Capron, I. King, S. Le Calvé, B. Alonso, J.-O. Durand, B. Bujoli, Z. Gan, G. Hoatson. *Magn. Reson. Chem.*, 2002, **40**, 70.
65. R.E. Wasylshen, S.E. Ashbrook, S. Wimperis, *NMR of Quadrupolar Nuclei in Solid Material*, Ed.; John Wiley & Sons Ltd., United Kingdom, 2012.
66. S.J. Clark, M.D. Segall, C.J. Pickard, P.J. Hasnip, M.J. Probert, K. Refson, M. Z. Payne., *Kristall.* 2005, **220**, 567.
67. C. D. Putnam, M. Hammel, G. L. Hura, and J. a Tainer, *Q. Rev. Biophys.*, 2007, **40**, 191.
68. H. Schnablegger and Y. Singh, *The SAXS Guide*, Anton Paar, Second Rev., 2011.
69. O. Glatter and O. Kratky, *Small Angle X-ray Scattering*, Academic Press Inc, New York, 1982.
70. P. B. Moore, *J. Appl. Crystallogr.*, 1980, **13**, 168.
71. Y. Hou, D. B. Fast, R. E. Ruther, J. M. Amador, L. B. Fullmer, S. R. Decker, L. N. Zakharov, M. Dolgos, and M. Nyman, *J. Solid State Chem.*, 2014, **Accepted**.
72. Y. Hou, L. N. Zakharov, and M. Nyman, *J. Am. Chem. Soc.*, 2013, **135**, 16651.

73. R. E. Ruther, B. M. Baker, J.-H. Son, W. H. Casey, and M. Nyman, *Inorg. Chem.*, 2014, **53**, 4234.
74. V. W. Day, W. G. Klemperer, and D. J. Maltbie, *J. Am. Chem. Soc.*, 1987, **109**, 299.
75. T. Kojima, M. R. Antonio, and T. Ozeki, *J. Am. Chem. Soc.*, 2011, **133**, 7248.
76. M. Nyman, T. M. Alam, F. Bonhomme, M. a. Rodriguez, C. S. Frazer, and M. E. Welk, *J. Clust. Sci.*, 2006, **17**, 197.
77. M. Nyman, F. Bonhomme, T. M. Alam, M. a Rodriguez, B. R. Cherry, J. L. Krumhansl, T. M. Nenoff, and A. M. Sattler, *Science*, 2002, **297**, 996.
78. F. Bonhomme, J. P. Larentzos, T. M. Alam, E. J. Maginn, M. Nyman, F. Hall, and N. Dame, *Inorg. Chem.*, 2005, **44**, 1774.
79. M. Nyman, J. P. Larentzos, E. J. Maginn, M. E. Welk, D. Ingersoll, H. Park, J. B. Parise, I. Bull, and F. Bonhomme, *Inorg. Chem.*, 2007, **46**, 2067.
80. Z. Zhang, Q. Lin, D. Kurunthu, T. Wu, F. Zuo, S. Zheng, C. J. Bardeen, X. Bu, and P. Feng, *J. Am. Chem. Soc.*, 2011, **2**, 6934.
81. R. P. Oleksak, R. E. Ruther, F. Luo, K. C. Fairley, S. R. Decker, W. F. Stickle, D. W. Johnson, E. L. Garfunkel, G. S. Herman, and D. A. Keszler, *Appl. Mater. Interfaces*, 2014, **6**, 2917.
82. G. M. Muha and P. a. Vaughan, *J. Chem. Phys.*, 1960, **33**, 194.
83. M. Aberg, *Acta Chem. Scand.*, 1977, **31**, 171.

84. D. M. Tiede, R. Zhang, L. X. Chen, L. Yu, and J. S. Lindsey, *J. Am. Chem. Soc.*, 2004, **126**, 14054.
85. R. Zhang, P. Thiagarajan, and D. M. Tiede, *J. Appl. Crystallogr.*, 2000, **33**, 565.
86. J. Lim, S. P. Yeap, H. X. Che, S. C. Low, *Nanoscale Res. Lett.*, 2013, **8**, 1.
87. S. E. Harden, *Biotechnol. Appl. Biochem.* 1986, **8**, 489.
88. T. Jian, S. H. Anastasiadis, A. K. Rizos, G. Fytasc, *J. Chem. Phys.*, 1994, **101**, 3222.
89. <http://www.intechopen.com/books/proteininteractions/characterization-of-protein-proteininteractions-via-static-and-dynamic-light-scattering>
90. <http://www.wyatt.com>
91. J. A. Dieringer et. al., *Faraday Discuss.*, 2006, **132**, 9.
92. M. E. Keating, H. J. Byrne, *Int. J. Nanomedicine*, 2013, **8**, 1335.
93. Mason, T.G.; Gang, H.; Weitz, D.A., *J. Opt. Soc. Am. A.* 1997, **14**, 139.
94. W. Wang, W. Liu, I.-Y. Chang, L. A. Wills, L. N. Zakharov, S. W. Boettcher, P. H.-Y. Cheong, C. Fang, D. A. Keszler, *PNAS* 2013, **110**, 1839.
95. (a) M. N. Jackson Jr, L. A. Willis, I.-Y. Chang, M. E. Carnes, L. Scatena, P. H.-Y. Cheong, D. W. Johnson, *Inorg. Chem.*, 2013, **52**, 6187. (b) M.K. Kamunde-Devonish, M.N. Jackson, Jr., Z.L. Mensinger, L.N. Zakharov, D.W. Johnson, *Inorg. Chem.* 2014, **53**, 7101.
96. W. W. Rudolph, R.; Mason, C. C. Pye, *Phys. Chem. Chem. Phys.* 2000, **2**, 5030.
97. X. López, J. J. Carbó, C. Bo, J. M. Poblet, *Chem. Soc. Rev.*, 2012, **41**, 7537.

98. A. J. Bridgeman, *Chem. Eur. J.* 2004, **10**, 2935.
99. X. López, J. M. Poblet, *Inorg. Chem.* 2004, **43**, 686.
100. H. El Moll, et al., *Chem. Eur. J.*, 2011, **17**, 14129.
101. B. Mennucci and J. Tomasi, *The Journal of Chemical Physics*, 1997, **106**, 5151–5158.
102. A. Klamt and G. Schüürmann, *J. Chem. Soc., Perkin Trans. 2*, 1993, 799–805.
103. R. Carr, I. A. Weinstock, A. Sivaprasadarao, A. Müller, *Nano Lett.*, 2008, **8**, 3916.
104. L. Vilà-Nadal, et al. *Phys. Chem. Chem. Phys.*, 2011, **13**, 20136.
105. L. Kronik, T. Stein, S. Refaely-Abramson and R. Baer, *J. Chem. Theory Comput.*, 2012, **8**, 1515–1531.
106. J. Gao, P. Amara, C. Alhambra, M. J. Field, *J. Phys. Chem. A.*, 1998, **102**, 4714.
107. A. Tongraar, K. R. Liedl, B. M. Rode, *J. Phys. Chem. A.*, 1998 **102**, 10340.
108. L. Kronik, T. Stein, *J. Chem. Theory Comput.*, 2012, **8**, 1515.
109. F. De Angelis, S. Fantacci, A. Selloni, M. K. Nazeeruddin, M. Grätzel, *J. Am. Chem. Soc.*, 2007, **129**, 14156.
110. J. F. Parker, K. A. Kacprzak, O. Lopez-Acevedo, H. Häkkinen, R. W. Murray, *J. Phys. Chem. C*, 2010, **114**, 8276.
111. X. López, C. Bo, J. M. Poblet, *J. Am. Chem. Soc.* 2002, **124**, 12574.
112. J. M. Maestre, X. Lopez, C. Bo, J.M. Poblet, C. A. Daul, *Inorg. Chem.*, 2002, **41**, 1883.

113. W. B. Kim, T. Voitl, G. J. Rodriguez-Rivera, J. A. Dumesic, *Science* 2004, **305**, 1280.
114. D. G. Truhlar, C. J. Cramer, A. Lewis, J. A. Bumpus, *J. Chem. Ed.* 2004, **81**, 596.
115. X. Jin, W. Yang, J. Tang, Y. Yan, W. Shi, S. Bi, *Dalton T.* 2012, **41**, 1027.
116. A. Bagno, M. Bonchio, J. Autschbach, *Chem. Eur. J.* 2006, **12**, 8460.



281x270mm (96 x 96 DPI)

This Perspective highlights several modern characterization techniques used to identify nanoscale inorganic clusters in the context of multiple case studies.